The Astrophysical Journal, 913:11 (16pp), 2021 May 20 https://doi.org/10.3847/1538-4357/abeefe

Targeting Bright Metal-poor Stars in the Disk and Halo Systems of the Galaxy

Guilherme Limberg[1], Rafael M. Santucci[2,3], Silvia Rossi[1], Derek Shank[4], Vinicius M. Placco[5], Timothy C. Beers[4], Kevin C. Schlaufman[6], Andrew R. Casey[7,8], Hélio D. Perottoni[1], and Young Sun Lee[9]
[1] Universidade de São Paulo, Instituto de Astronomia, Geofísica e Ciências Atmosféricas, Departamento de Astronomia, SP 05508-090, São Paulo, Brazil
guilherme.limberg@usp.br
[2] Universidade Federal de Goiás, Instituto de Estudos Socioambientais, Planetário, Goiânia, GO 74055-140, Brazil
[3] Universidade Federal de Goiás, Campus Samambaia, Instituto de Física, Goiânia, GO 74001-970, Brazil
[4] Department of Physics and JINA Center for the Evolution of the Elements, University of Notre Dame, Notre Dame, IN 46556, USA
[5] Community Science and Data Center/NSFs NOIRLab, 950 N. Cherry Avenue, Tucson, AZ 85719, USA
[6] Department of Physics and Astronomy Johns Hopkins University 3400 North Charles Street Baltimore, MD 21218, USA
[7] School of Physics & Astronomy, Monash University, Wellington Road, Clayton 3800, Victoria, Australia
[8] ARC Centre of Excellence for All Sky Astrophysics in 3 Dimensions (ASTRO 3D), Canberra, ACT 2611, Australia
[9] Department of Astronomy and Space Science, Chungnam National University, Daejeon 34134, Republic Of Korea
Received 2021 February 1; revised 2021 March 12; accepted 2021 March 12; published 2021 May 18

Abstract

We present the results of spectroscopic follow-up for 1897 low-metallicity star candidates, selected from the Best & Brightest (B&B) Survey, carried out with the GMOS-N/S (Gemini North/South telescopes) and Goodman (SOAR Telescope) spectrographs. From these low-resolution ($R \sim 2000$) spectra, we estimate stellar atmospheric parameters, as well as carbon and magnesium abundance ratios. We confirm that 56% of our program stars are metal-poor ([Fe/H] < -1.0), 30% are very metal-poor (VMP; [Fe/H] < -2.0), and 2% are extremely metal-poor (EMP; [Fe/H] < -3.0). There are 191 carbon-enhanced metal-poor (CEMP) stars, resulting in CEMP fractions of 19% and 43% for the VMP and EMP regimes, respectively. A total of 94 confirmed CEMP stars belong to Group I (A(C) $\gtrsim 7.25$) and 97 to Group II (A(C) $\lesssim 7.25$) in the Yoon–Beers A(C)−[Fe/H] diagram. Moreover, we combine these data with Gaia EDR3 astrometric information to delineate new target-selection criteria, which have been applied to the Goodman/SOAR candidates, to more than double the efficiency for identification of bona fide VMP and EMP stars in comparison to random draws from the B&B catalog. We demonstrate that this target-selection approach can achieve success rates of 96%, 76%, 28%, and 4% for [Fe/H] $\leqslant -1.5$, $\leqslant -2.0$, $\leqslant -2.5$ and $\leqslant -3.0$, respectively. Finally, we investigate the presence of dynamically interesting stars in our sample. We find that several VMP/EMP ([Fe/H] $\leqslant -2.5$) stars can be associated with either the disk system or halo substructures like Gaia-Sausage/Enceladus and Sequoia.

Unified Astronomy Thesaurus concepts: Population II stars (1284); Milky Way stellar halo (1060); Milky Way disk (1050); CEMP stars (2105); Spectroscopy (1558); Chemical abundances (224); Stellar atmospheres (1584); Milky Way dynamics (1051); Milky Way evolution (1052); Milky Way formation (1053)

Supporting material: machine-readable tables

1. Introduction

Very metal-poor (VMP; [Fe/H][10] < -2.0) and extremely metal-poor (EMP; [Fe/H] < -3.0) stars are relics of the formation and evolution of the Galaxy, providing clues on the nucleosynthesis processes operating throughout its early history (Beers & Christlieb 2005). Seminal efforts, focused toward discovering VMP and EMP stars in the past, e.g., the HK survey (Beers et al. 1985, 1992) and the Hamburg/ESO survey (Christlieb 2003; Christlieb et al. 2008), provided the majority of targets observed at high spectroscopic resolution over the last few decades (e.g., Norris et al. 1996; Hill et al. 2002; Cayrel et al. 2004; Aoki et al. 2007; Cohen et al. 2008; Yong et al. 2013a; Roederer et al. 2014). Studies of these ancient stars have allowed stellar archaeologists to constrain the conditions for the chemical enrichment of the star-forming environments that existed in the nascent Milky Way (Frebel & Norris 2015).

Beers et al. (1992) first noted the presence of a surprisingly large number of carbon-enhanced stars among their sample at the lowest metallicities. As the sample sizes increased, it was recognized that the fraction of carbon-enhanced metal-poor (CEMP; [C/Fe] $> +0.7$ and [Fe/H] < -1.0) stars indeed rapidly increases with decreasing [Fe/H] (Norris et al. 1997; Rossi et al. 1999, 2005; Lucatello et al. 2006; Lee et al. 2013; Yong et al. 2013b; Placco et al. 2014b; Yoon et al. 2018) and at greater distances from the Galactic plane ($|Z|_{\rm Gal}$; Frebel et al. 2006; Carollo et al. 2012; Lee et al. 2017, 2019; Yoon et al. 2018). This behavior has been proposed to be related to the dual nature of the stellar halo (Carollo et al. 2007, 2010; Beers et al. 2012), hereafter simply referred to as the "halo." It has been suggested that the majority of the CEMP stars in the [Fe/H] $\lesssim -2.5$ regime belong to the CEMP-no subclass, showing no enhancements in neutron-capture elements ([Ba/Fe] < 0.0; see Yoon et al. 2016, 2019). These observations support the hypothesis that the CEMP-no stars are the direct descendants of massive Population III stars that are now long vanished (Ryan et al. 2005; Aoki et al. 2007; Ito et al. 2013; Spite et al. 2013; Keller et al. 2014; Tominaga et al. 2014; Frebel et al. 2015; Roederer et al. 2016; Placco et al. 2016a, 2016b; Aguado et al. 2018; Ezzeddine et al. 2019).

Another peculiarity found in the chemical-abundance profiles of some metal-poor stars is their enhancement in

[10] Definition of elemental abundances for a star ($\star$) relative to the Sun ($\odot$): [A/B] $= \log(N_{\rm A}/N_{\rm B})_{\star} - \log(N_{\rm A}/N_{\rm B})_{\odot}$, where $N_{\rm A}$ ($N_{\rm B}$) is the number density of atoms of element A (B). The adopted composition of the Sun is from Asplund et al. (2009).

r-process (rapid neutron capture) elements; see Sneden et al. (2008) and Frebel (2018) for reviews on the topic. The qualitative aspects of the formation of these neutron-rich nuclei have been known for many decades (e.g., Burbidge et al. 1957; Cameron 1957). However, the astrophysical site(s) in which the *r*-process occurs remained speculative up until the photometric and spectroscopic observations of the electromagnetic counterpart AT2017gfo (Arcavi et al. 2017; Drout et al. 2017; Pian et al. 2017; Shappee et al. 2017; Smartt et al. 2017) of the gravitational wave event GW170817 (Abbott et al. 2017a, 2017b, 2017c) of a neutron star merger. These authors concluded that this transient (kilonova) was powered by the radioactive decay of large amounts of *r*-process elements, in agreement with early theoretical predictions (Lattimer & Schramm 1974). It has been suggested that neutron star mergers are the primary (and perhaps the only) source of *r*-process enrichment in the Galaxy (e.g., Côté et al. 2018; Safarzadeh et al. 2019a; Banerjee et al. 2020; Dvorkin et al. 2020), but other studies (Belczynski et al. 2018; Ji & Frebel 2018; Ji et al. 2019; Côté et al. 2019; Safarzadeh et al. 2019b; Haynes & Kobayashi 2019; Kobayashi et al. 2020) have provided evidence that additional sources may be involved.

In the Gaia era, proper motions (PMs) and parallaxes of exquisite quality have been made available for more than a billion stars (Gaia Collaboration et al. 2016a). The phase-space information, particularly from Gaia Data Release 2 (DR2; Gaia Collaboration et al. 2018), combined with previously available high-resolution spectroscopic data, has enabled the exploration of the chemo-dynamical properties of these low-metallicity stars. It has been revealed that a large population of EMP and ultra metal-poor (UMP; [Fe/H] < -4.0) stars are apparently kinematically connected (similar $|Z|_{\rm Gal}$ and rotational motion around the Galactic center) to the disk system (Sestito et al. 2019, 2020; Cordoni et al. 2021), providing constraints on the assembly of the newborn Milky Way (redshift $z \gtrsim 2$) through its primordial building blocks (Di Matteo et al. 2020; Sestito et al. 2021).

Considering all of the abovementioned advances, it is clear that numerous VMP and EMP stars are necessary to advance our understanding of the formation and evolution of the Galaxy. The pioneering objective-prism surveys (Bond 1970, 1980; Bidelman & MacConnell 1973; Beers et al. 1985, 1992; Christlieb 2003; Christlieb et al. 2008) have been responsible for the identification of thousands of VMP stars and several hundred EMP stars. Large spectroscopic surveys such as the Sloan Digital Sky Survey (SDSS; York 2000) and its stellar-specific subsurvey Sloan Extension for Galactic Understanding and Exploration (SEGUE; Yanny et al. 2009), the Large Sky Area Multi-object Fiber Spectroscopic Telescope (LAMOST; Cui et al. 2012; Zhao et al. 2012; see also Li et al. 2018b), and the Radial Velocity Experiment (RAVE; Steinmetz et al. 2006) have increased these numbers to tens of thousands of VMP and several thousand EMP stars. Ongoing and planned spectroscopic surveys in the near future, including WEAVE (Dalton et al. 2012), 4MOST (de Jong et al. 2012, 2014), Pristine (Starkenburg et al. 2017b; Aguado et al. 2019; Youakim et al. 2020), H3 (Conroy et al. 2019a, 2019b), and SDSS-V/MWM (Kollmeier et al. 2017), are expected to expand these numbers further.

More recently, the Best & Brightest (B&B) initiative (Schlaufman & Casey 2014; see also Casey & Schlaufman 2015; Reggiani et al. 2020) has taken advantage of mid-infrared photometry from the Wide-field Infrared Survey Explorer (WISE; Wright et al. 2010) mission, in combination with near-infrared photometry from the Two Micron All Sky Survey (2MASS; Skrutskie et al. 2006), to select almost 12,000 low-metallicity candidates. From follow-up spectroscopy of ∼200 objects in this list, those authors obtained efficiencies of 33% and 4% in finding VMP and EMP stars, respectively. Placco et al. (2019), hereafter P19, have incorporated magnitude (in the *V*-band), reddening ($E(B-V)$), and PM cuts in the target selection of their own follow-up of stars from the B&B catalog. The more restrictive criteria yielded similar success rates, 42% (VMP) and 2% (EMP), for their much larger sample of ∼800 candidates, but including fainter targets. The VMP and EMP stars uncovered through the B&B selection have served as targets for high-resolution spectroscopy conducted by the *R*-Process Alliance (e.g., Holmbeck et al. 2020 and references therein), as they are all brighter than $V = 14$ and can be readily observed with 2.5–6.5 m class telescopes from the ground.

With the advent of Gaia, we have the opportunity to combine astrometric (as discussed in Placco et al. (2018), hereafter P18) and photometric (WISE+2MASS/B&B) information to increase the efficiency in identifying VMP and EMP stars. This should allow us to populate the carbon- and *r*-process-enhanced classes of metal-poor stars with bright objects much faster, enabling studies of their origins, constraining supernovae nucleosynthesis and chemical evolution models, and probing rare, chemically peculiar targets for future investigations.

The goal of the present work is to identify VMP and EMP stars from the B&B catalog, confirming (or disconfirming) their metal-poor nature via low-resolution ($R \sim 2000$) spectroscopy. We also seek to determine carbon and magnesium (representative of the α elements) abundances. Crucially, we incorporate Gaia Early Data Release 3 (EDR3; Gaia Collaboration et al. 2021) astrometry to investigate the effect of kinematic-based target selection on the success rates of finding low-metallicity stars. These criteria can be taken into account for ongoing and future searches for metal-poor stars in the Galaxy. The most interesting VMP and EMP stars vetted by this approach will serve as targets for ongoing and forthcoming high-resolution spectroscopic campaigns. Finally, we revisit the behaviors of VMP star fractions, as functions of both $|Z|_{\rm Gal}$ and velocities, and the increase of CEMP star fractions with declining metallicity. We also investigate the dynamically interesting VMP/EMP stars with either disk- or halo-like orbits.

This paper is outlined as follows. In Section 2, details of target selection, observations, and data reduction are provided. Section 3 is dedicated to the estimation of stellar atmospheric parameters: effective temperature ($T_{\rm eff}$), surface gravity ($\log g$), and metallicity (as represented by [Fe/H]), and also elemental abundances of interest ([C/Fe] and [Mg/Fe]). We explore the behaviors of these abundance ratios as functions of [Fe/H] in Section 4. In Section 5, we investigate the kinematics of the selected low-metallicity candidates and examine the improvements in the efficiency of finding VMP stars in the Galaxy. We also analyze the orbits of VMP/EMP, in Section 5, in the context of the recent literature. Finally, Section 6 presents a summary of our conclusions.

2. Target Selection, Observations, and Data Reduction

All of our targets have been selected as metal-poor candidates by Schlaufman & Casey (2014) as part of the B&B Survey. A total of 1897 stars have been observed with either the Gemini Multi-Object Spectrographs (GMOS-N/S; Davies et al. 1997; Gimeno et al. 2016) or Goodman spectrograph (Clemens et al. 2004) at the

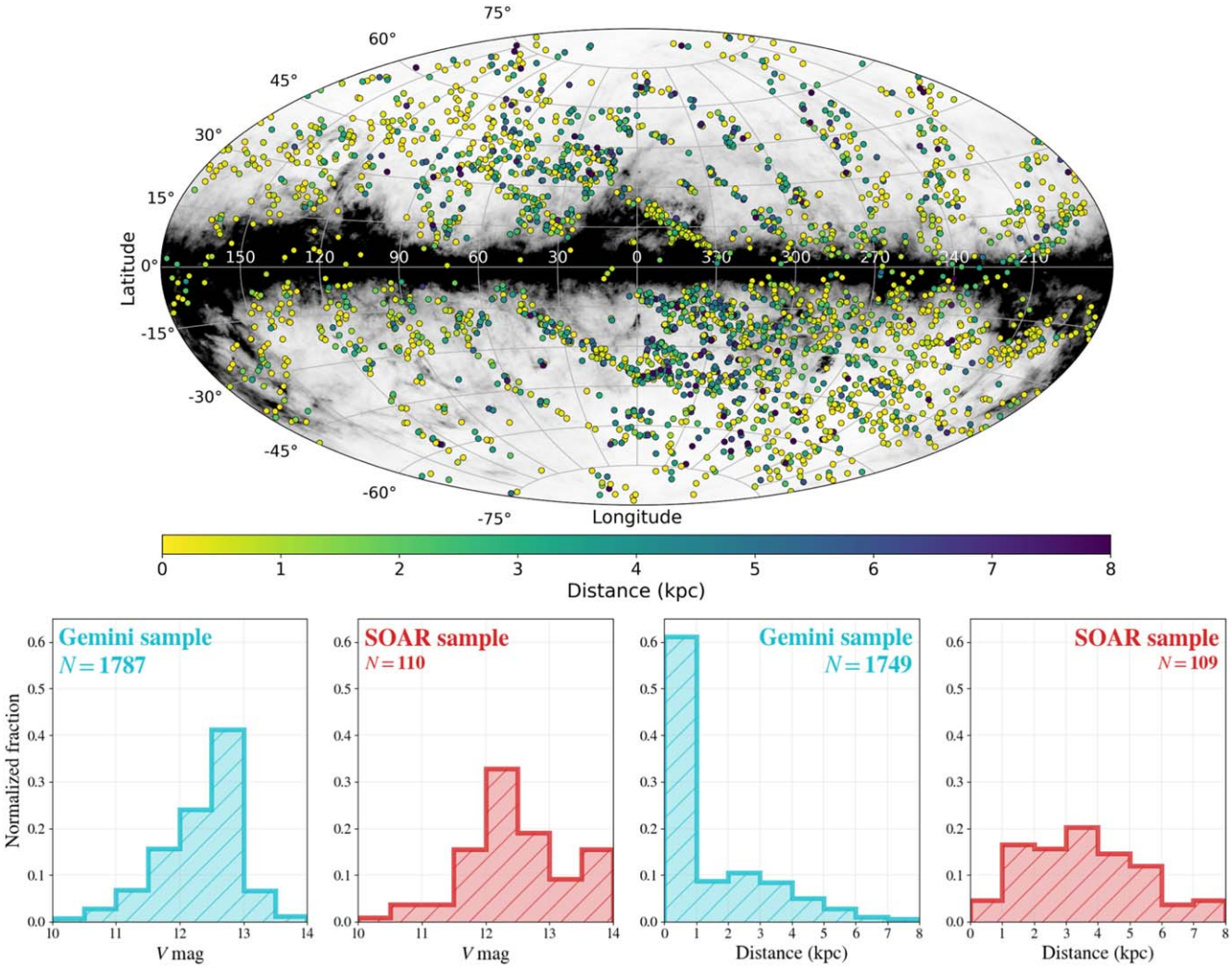

Figure 1. Top panel: distribution of the Gemini (Section 2.1), SOAR (Section 2.2), and P19 samples in the Galactic coordinate system, color-coded by heliocentric distances (Section 5). The background all-sky distribution of the Galactic reddening comes from the Schlegel et al. (1998) dust map, as recalibrated by Schlafly & Finkbeiner (2011). The different gray scales represent $E(B-V)$ values from 0.0 (white) to 0.5 (black). Bottom panels: distributions of V-band magnitudes (Section 2) and heliocentric distance estimates (Section 5) for the Gemini (cyan) and SOAR samples (red). Total number of stars represented in each histogram is also shown in each respective panel.

Gemini (North/South; 8.1 m) and the Southern Astrophysical Research (SOAR; 4.1 m) telescopes, respectively. By design, all candidates are significantly bright ($V \lesssim 14.0$; bottom left panels of Figure 1), which makes them excellent for high-resolution follow-up. The typical signal-to-noise ratio (S/N) of our spectra is $\gtrsim$30 per pixel at the wavelength region of the Ca II K/H lines (3900–4000 Å). Since the target-selection criteria were different for observations with each instrument, we divide our stars into a "Gemini sample" (Section 2.1) and a "SOAR sample" (Section 2.2). The calibrations included bias frames, quartz flats, and arc-lamp exposures. The background subtraction, definition of aperture, extraction of the one-dimensional spectra, and wavelength calibrations for each spectrum have been conducted with standard `IRAF` (Tody 1986, 1993) packages.

Pertinent observational information for the stars in our samples are presented in Table 1, including 2MASS names and Gaia EDR3 (Gaia Collaboration et al. 2021) IDs and coordinates. The different telescopes and instruments are also listed. Table 2 includes relevant photometric information: V, G, and J magnitudes, and $B-V$, $G_{BP}-G_{RP}$, and $J-K$ colors from the AAVSO Photometric All Sky Survey (APASS; Henden & Munari 2014) DR9, Gaia EDR3 (Riello et al. 2021), and 2MASS, respectively. The reddening values (Table 2) have been estimated with the Schlegel et al. (1998) dust maps (top panel of Figure 1). These can be easily recalibrated into other $E(B-V)$ systems (e.g., Schlafly & Finkbeiner 2011).

2.1. The Gemini Sample

The majority (1787/1897; 94%) of the spectra were acquired with the GMOS-N and GMOS-S spectrographs at Gemini North and South, respectively. The observations in this program were obtained between 2014A and 2019B; the various proposal IDs are listed in Table 1. All observations used 0.″5 slits. During semesters 2014A, 2015A, and 2015B, the spectra were obtained with the B1200 l mm^{-1} G5301 (North) and G5321 (South) gratings, which led to a resolving power of $R \sim 2400$–2800. For all other observing runs, we have employed the B600 l mm^{-1} G5307 (North) and G5323 (South) gratings, resulting in $R \sim$ 2000–2600. The typical wavelength coverage of GMOS-N/S spectra is 3200–5800 Å. We have been able to obtain stellar-parameter estimates for all but five stars in this sample (Section 3). The cases for which we have not been able to estimate $T_{\rm eff}$ and

Table 1
Coordinates and Observing Details

Star Name (2MASS)	Star Name (Gaia EDR3)	R.A. (deg)	Decl. (deg)	l (deg)	b (deg)	Telescope	Instrument	Program ID
00003305−7953389	4634573766005607552	0.1375	−79.8942	305.7037	−36.9587	SOAR	Goodman	SO-2019B-013
00020162−4430117	4994519032163925632	0.5067	−44.5033	329.4221	−69.9972	SOAR	Goodman	SO-2019B-013
00040305−6106367	4905632480654004608	1.0127	−61.1102	312.9121	−55.0903	Gemini South	GMOS-S	GS-2016A-Q-76
00043646 + 4124062	384060304935385984	1.1519	41.4017	113.5728	−20.6174	Gemini North	GMOS-N	GN-2017B-Q-75
00045403 + 3524010	2876804519751163008	1.2251	35.4003	112.3464	−26.5131	Gemini North	GMOS-N	GN-2016A-Q-75

(This table is available in its entirety in machine-readable form.)

Table 2
Colors, Magnitudes, and Reddening Estimates

Star Name (2MASS)	Star Name (Gaia EDR3)	V	$(B-V)$	G	$(G_{BP}-G_{RP})$	J	$(J-K)$	$E(B-V)$
00003305−7953389	4634573766005607552	12.411	0.775	12.184	1.069	10.804	0.535	0.074
00020162−4430117	4994519032163925632	12.631	0.807	12.397	1.067	11.007	0.567	0.011
00040305−6106367	4905632480654004608	12.818	1.075	12.417	1.466	10.546	0.745	0.010
00043646 + 4124062	384060304935385984	12.612	1.025	12.371	1.082	10.896	0.643	0.073
00045403 + 3524010	2876804519751163008	12.174	0.698	11.925	1.011	10.576	0.513	0.063

(This table is available in its entirety in machine-readable form.)

log g were due to low-S/N ($\lesssim$10 per pixel at ∼4000 Å) spectra and/or large mismatches between the color-based temperatures and the spectroscopic calibrations, which is expected for stars outside the $4000 \leqslant T_{\rm eff}\,({\rm K}) \leqslant 7000$ range.

2.2. The SOAR Sample

Unlike the Gemini sample, stars in the SOAR sample took into account phase-space information in the target selection. In P18, PMs from Gaia DR1 (Gaia Collaboration et al. 2016b) and line-of-sight[11] velocities ($V_{\rm los}$) from the RAVE DR5 (Kunder et al. 2017) had already been used to explore this possibility. The success rate in finding low-metallicity ([Fe/H] $\lesssim -1.5$) stars was higher for both larger $|Z|_{\rm Gal}$ and transverse velocities relative to the Sun ($V_{\rm T}$). Here, we develop this idea further, and propose an improved, more robust set of criteria. In order to take full advantage of both PMs and $V_{\rm los}$ from Gaia's past and future DRs, we introduce the quantity "total available velocity" ($V_{\rm TAV}$), where:

$$V_{\rm TAV} = \begin{cases} (V_{\rm los}^2 + V_{\rm T}^2)^{1/2} \text{ if } V_{\rm los} \text{ and } V_{\rm T} \text{ are available;} \\ V_{\rm T} \text{ if only proper motions are available;} \\ V_{\rm los} \text{ if only this component is available.} \end{cases} \quad (1)$$

A detailed description, along with the advantages and limitations of the $V_{\rm TAV}$ parameter, is given in Section 5.1. From this definition, the candidates in the SOAR sample have been selected according to: $|Z|_{\rm Gal} > 0.5$ kpc and $V_{\rm TAV} > 100$ km s^{-1}, derived from the Gaia DR2 data available at the time of observations. In Section 5.2, we provide an in-depth exploration of the $Z_{\rm Gal}$ versus $V_{\rm TAV}$ diagram, justifying these choices.

With Goodman/SOAR, 110 (6% of the complete sample) metal-poor candidates were observed over the course of the 2018B and 2019B semesters (Table 1). The instrumental setup was similar to the one described in Section 2.1, including a 600 l mm^{-1} grating and a 1.″0 long slit. The typical wavelength coverage for Goodman/SOAR spectra is 3600–6200 Å, and the achieved resolution is $R \sim 1300$. For the SOAR sample, stellar parameters have been derived for all but two stars.

3. Stellar Parameters and Abundances

In order to determine the stellar atmospheric parameter values ($T_{\rm eff}$, log g, and [Fe/H]), we have followed the same approach as P18, P19, and Limberg et al. (2021), where the fundamental proxy for metallicity is the Ca II K line (∼3933 Å). We have employed the n-SSPP (Beers et al. 2014, 2017), a customized version of the Segue Stellar Parameter Pipeline (SSPP; Lee et al. 2008a, 2008b, 2011, 2013). This methodology consists of several routines (e.g., photometric calibrations and spectral-line indices) to derive estimates of the stellar parameters. It also compares the input spectra with a dense grid of synthetic ones in a χ^2 minimization framework. The best set of values is then adopted, taking into account the wavelength coverage of the analyzed spectrum, its S/N, and calculated uncertainties.

Considering both samples, the atmospheric parameters have been determined for all but seven stars (out of 1897; see Table 3), as mentioned in Section 2. Based on empirical comparisons with high-resolution spectroscopic analyses (Placco et al. 2014a; Beers et al. 2014, 2017), the typical errors for $T_{\rm eff}$, log g, and [Fe/H] are ±150 K, ±0.35 dex and ±0.20 dex, respectively, for S/N ∼ 30 per pixel at ∼4000 Å. These estimated atmospheric parameters can be visualized in Figure 2, where the log g versus $T_{\rm eff}$ distribution is overlapped by MESA Isochrones and Stellar Tracks (MIST; Dotter 2016; Choi et al. 2016) models with varying metallicities. Overall, we have confirmed that 1064 (56^{+2}_{-2}%[12]) of

[11] Throughout this work, we employ the "line-of-sight" terminology instead of the more common "radial velocity" nomenclature. We reserve the latter for the radial component of the Galactocentric velocities in the cylindrical coordinate frame (see Section 5.3).

[12] Uncertainties in the fractions are given by the Wilson (1927) score approximation, which provides an estimate of the binomial proportion confidence intervals. This approximation is commonly used for small-number statistics ($n \lesssim 40$), but is also comparable to other metrics when the analyzed sample is larger.

Table 3
Stellar Atmospheric Parameters and Abundances

Star Name (2MASS)	Star Name (Gaia EDR3)	$T_{\rm eff}$ (K)	$\log g$ (cgs)	[Fe/H]	[C/Fe]	$[C/Fe]_c$	$A(C)_c$	[Mg/Fe]
00003305−7953389	4634573766005607552	5280	2.06	−1.93	+0.13	+0.17	6.67	+0.38
00020162−4430117	4994519032163925632	5036	2.00	−1.81	+0.30	+0.37	6.99	···
00040305−6106367	4905632480654004608	4648	4.13	−1.27	+0.15	+0.15	7.31	−0.19
00043646 + 4124062	384060304935385984	6068	3.51	−1.29	+0.95	+0.95	8.09	+0.14
00045403 + 3524010	2876804519751163008	5455	3.52	−2.59	+0.50	+0.50	6.34	+0.06

Note. $[C/Fe]_c$ and $A(C)_c$ values have been corrected for evolutionary status (Placco et al. 2014b).
(This table is available in its entirety in machine-readable form.)

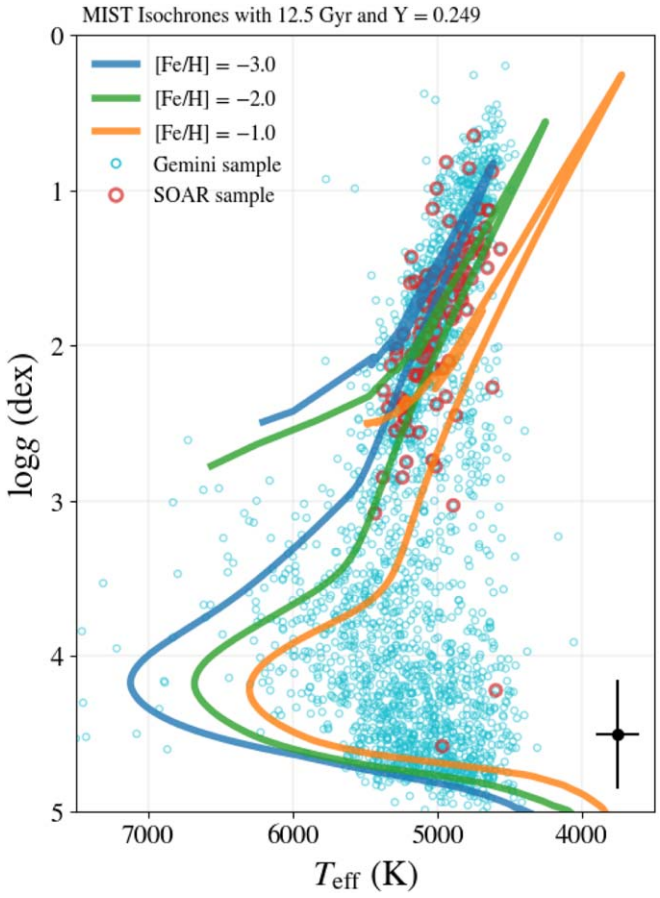

Figure 2. $T_{\rm eff}$ vs. $\log g$ diagram of the Gemini (cyan circles; Section 2.1) and SOAR (red symbols; Section 2.2) samples. Typical uncertainties for these atmospheric parameters (±150 K for $T_{\rm eff}$ and ±0.35 dex for $\log g$; Section 3) are represented by the black dot with error bars in the bottom right corner. Colored lines are MIST isochrones with varying metallicities (Dotter 2016; Choi et al. 2016). Orange, green, and blue isochrones represent [Fe/H] = −1.0, −2.0, and −3.0, respectively. At the top, we list the rest of the conditions employed to generate the MIST stellar population models: Age = 12.5 Gyr and $Y = 0.249$ (primordial He abundance; Planck Collaboration et al. 2016).

the newly observed stars are metal-poor ([Fe/H] < −1.0), 566 (30^{+2}_{-2}%) are VMP, and 35 (2^{+1}_{-1}%) are EMP. These are very similar proportions to what had been previously achieved by both Schlaufman & Casey (2014) and P19, who used similar selection functions while performing spectroscopic follow-up on targets from the B&B Catalog. We emphasize that, although the targets observed at SOAR were chosen from kinematic criteria, these represent only a small portion of the complete (Gemini+SOAR) sample, hence these comparisons remain valid.

With the n-SSPP pipeline application, we have also obtained [C/Fe] estimates for most stars from both samples. The carbon-to-iron ratios are estimated from the strength of the CH *G*-band molecular feature (∼4300 Å). We have also calculated corrections for the [C/Fe] (and $A(C)$[13]) following the prescriptions of Placco et al. (2014b). Those authors employed stellar evolution models (Stancliffe et al. 2009) to account for the intrinsic carbon depletion (with consequent enhancement in nitrogen) in the atmospheres of metal-poor stars due to mixing with internal layers of material enriched by the CN cycle during the red giant branch phase (Charbonnel 1995). The corrected carbon-abundance values are indicated by $[C/Fe]_c$ (or $A(C)_c$) throughout this work, and are listed in Table 3. We also note that metallicities and carbon abundances of cooler ($T_{\rm eff} \lesssim 4500$ K) CEMP stars found in this work (and other low-resolution efforts) might be severely affected by the presence of "carbon-veiling," which depresses the continuum in the wavelength region of the Ca II K/H lines, hindering the metallicity determination (see discussion in Yoon et al. (2020)). The accuracy for [C/Fe] (and $[C/Fe]_c$) is 0.20 dex (Lee et al. 2013; Beers et al. 2014, 2017).

The n-SSPP derives the abundances of magnesium from the Mg I triplet absorption lines (located in the range of 5150–5200 Å). For the Gemini sample, Mg-to-iron ratios have been obtained for 1104/1787 (62%) of the stars. For the SOAR sample, 85/110 (77%) stars had [α/Fe] estimated. The cases for which these abundances are not determined are due to low-quality (S/N $\lesssim$ 10) spectra or to absorption features that are too weak to be distinguished from the underlying noise. The typical errors for [Mg/Fe] are also 0.20 dex (Lee et al. 2011; P18, P19). The [Mg/Fe] ratios are listed in Table 3.

4. Carbon and α- elements

Carbon-to-iron ratios in low-metallicity stars can constrain their different formation scenarios (see, e.g., Aoki et al. 2002, 2007; Nomoto et al. 2013; Hansen et al. 2016). The α-element abundances are crucial for our classical understanding of Galactic chemical evolution (e.g., Chiappini et al. 1997). Furthermore, the Mg-to-carbon ([Mg/C]) ratio serves as a diagnostic for the so-called "mono-enriched" population ([Fe/H] $\lesssim -2.5$ and [Mg/C] $\lesssim -1.0$; Hartwig et al. 2018; see also Rasmussen et al. (2020)) which are, potentially, genuine second-generation stars. Figure 3 provides plots of the [Mg/Fe] and $A(C)_c$ distributions as functions of [Fe/H] (left and right panels, respectively).

[13] Absolute abundance. $A(X) = \log \epsilon(X) = \log(N_X/N_H) + 12$, where N_X and N_H are the number density of atoms of the given element and of hydrogen, respectively.

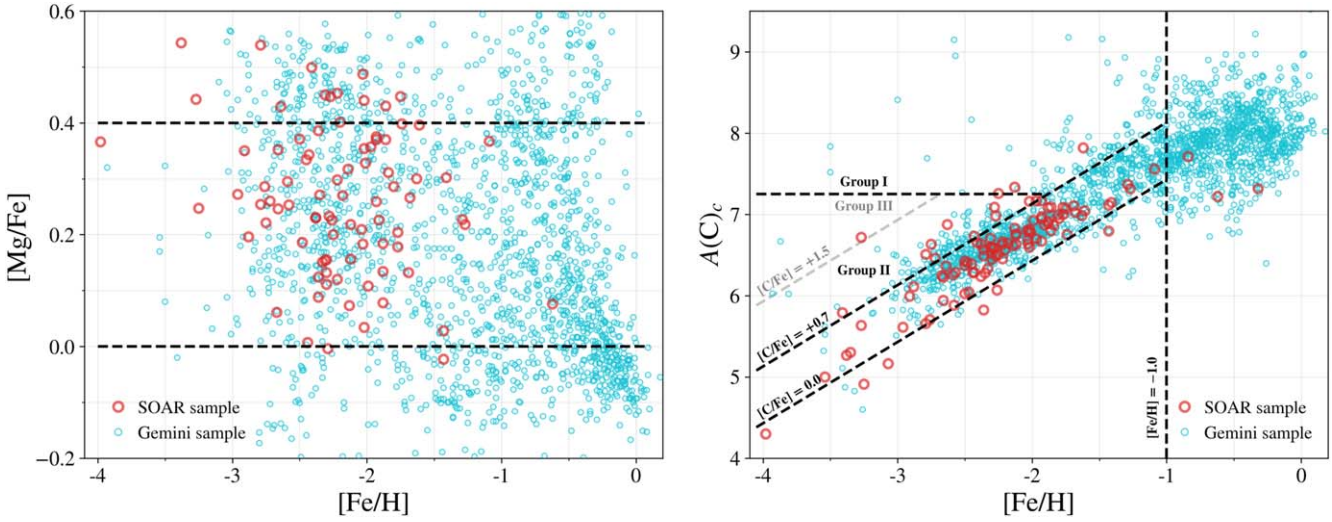

Figure 3. Left panel: Mg-to-iron ratio ([Mg/Fe]; Section 4) vs. metallicity ([Fe/H]; Section 3). Dashed lines mark different levels of Mg enrichment. Cyan and red open circles correspond to stars in the Gemini (Section 2.1) and SOAR (Section 2.2) samples, respectively, in a color scheme similar to those of Figures 1 and 2. Right panel: absolute carbon abundance ($A(C)_c$; Section 4), corrected for evolutionary effects (Placco et al. 2014b), vs. [Fe/H] diagram. Black dashed lines mark the classification for different levels of carbon enhancement according to Yoon et al. (2016, 2019) and considered in this work; see text for details. For convenience, we mark the characteristic region of Group III with a gray line. Vertical line marks the metal-poor limit at [Fe/H] = −1.0, for reference.

We first discuss the α-element abundances. Within the wavelength coverage and resolution of our spectra, the estimated [Mg/Fe] is the main representative of the α process. In the metal-rich regime, there is an accumulation of stars at [Mg/Fe] ~ 0.0 and [Fe/H] $\gtrsim -0.5$, associated with the (low-α) thin disk. We also note the presence of stars related to the (high-α) thick disk at [Mg/Fe] $\sim +0.3$ and [Fe/H] $\gtrsim -1.0$. Since we focus on metal-poor stars, further exploration of these components is beyond the scope of the present work. All estimated magnesium-to-iron ratios are in the range $-0.2 <$ [Mg/Fe] $< +0.6$, which is expected from Galactic chemical-evolution models based on high-precision spectroscopy of α elements (Zhao et al. 2016; Reggiani et al. 2017).

Regarding the carbon abundances, we have explored the Yoon-Beers A(C) versus [Fe/H] diagram, following the suggested classification of Yoon et al. (2016, 2019). For consistency, we have applied the criteria outlined by P18, also employed in P19, presented in Figure 3 (dashed lines). Besides the [Fe/H] < -1.0 and $[C/Fe]_c > +0.7$ conditions, we consider CEMP stars to be members of the so-called Group I if $A(C)_c \gtrsim 7.25$. Since the carbon enrichment of these stars' atmospheres is usually accompanied by enhancement in their abundances of slow neutron-capture (s-process) elements (Spite et al. 2013; Bonifacio et al. 2015; Hansen et al. 2015; Cruz et al. 2018), they are generally associated with the CEMP-s ([Ba/Fe] $> +1.0$ and [Ba/Eu] $> +0.5$; Beers & Christlieb 2005) subclass of CEMP stars. Such a chemical profile is thought to be the result of mass transfer from a binary companion in the asymptotic giant branch (AGB) phase (Suda et al. 2004; Ryan et al. 2005; Lucatello et al. 2005; Bisterzo et al. 2011; Allen et al. 2012; Placco et al. 2013; Starkenburg et al. 2014; Hansen et al. 2016). On the other hand, CEMP stars with $A(C)_c \lesssim 7.25$ are classified as Group II. Unlike the CEMP-s category, these low-A(C) objects do not present over-abundances of s-process elements ([Ba/Fe] < 0.0; Beers & Christlieb 2005), and are known as CEMP-no stars. This abundance pattern is the result of pollution of these stars' birth environments through a single EMP (perhaps metal-free; see Heger & Woosley (2010)) core-collapse supernovae episode; for a review, see Nomoto et al. (2013). Typically, the A(C) versus [Fe/H] diagram is further partitioned with a Group III, analogous to Group II, but with $[C/Fe]_c \gtrsim +1.5$ (Yoon et al. 2016, 2019). Those same authors argued that CEMP-s and CEMP-no stars could be distinguished from A(C) alone with $\sim$90% purity. We also note that the Group III stars are generally found at the lowest metallicities ([Fe/H] $\lesssim -3.0$), for which we have only a handful of stars in our samples (Section 3). Hence, for simplicity, we have not considered the Group III classification in this work.

We have confirmed that a total of 191 stars in the Gemini +SOAR sample are CEMP stars.[14] Out of these, 94 belong to the (Group I) CEMP-s subclass, according to the criteria described above. The remaining 97 of our CEMP stars can be classified as Group II (CEMP-no). From Figure 3, one can see that not only does the overall fraction of CEMP stars increase with decreasing metallicity, the CEMP-no class also dominates the [Fe/H] $\lesssim -2.3$ regime, similarly to the case in Yoon et al. (2018), which is in line with the expectation that the emergence of CEMP-s stars in the Galaxy is driven by AGB evolution (Herwig 2005) timescales. On the other hand, all CEMP stars above [Fe/H] $\gtrsim -1.8$ are CEMP-s (Group I).

Finally, we have confirmed the trend of increasing CEMP star fractions as a function of declining metallicity. For [Fe/H] < -2.5, we have found a CEMP star fraction of 32^{+6}_{-6}%, compatible (1σ) with both P19 and Schlaufman & Casey (2014). We have also found excellent agreement between our results, those from P19, and the high-resolution effort of Placco et al. (2014b). For [Fe/H] < -2.0, we have obtained 19^{+3}_{-3}%. In the [Fe/H] < -3.0 regime, for which we have very few stars, we have calculated 43^{+16}_{-15}%.

5. Kinematics of the Metal-poor Candidates

Astrometry can be used to improve the efficiency in the search for VMP stars in the Galaxy. In P18, the Tycho-Gaia

[14] Note that CEMP stars can be further divided into the CEMP-r ([Eu/Fe] $> +0.3$ and [Ba/Eu] < 0.0) and CEMP-r/s or CEMP-i ($0.0 <$ [Ba/Eu] $> +0.5$) categories (Hansen et al. 2018; Ezzeddine et al. 2020). However, these are not considered in this work, given the impossibility of classifying them without knowledge of their Ba and Eu abundances.

Table 4
Phase-space Information from Gaia EDR3

Star Name (2MASS)	Star Name (Gaia EDR3)	V_{los} (km s^{-1})	d_{helio} (kpc)	σ_d (kpc)	$PM_{R.A.}$ (mas yr^{-1})	$PM_{Decl.}$ (mas yr^{-1})	Z_{Gal} (kpc)	V_{TAV} (km s^{-1})
00003305−7953389	4634573766005607552	269.3	2.51	0.06	−4.538	−4.538	−1.48	274.3
00020162−4430117	4994519032163925632	58.5	3.13	0.19	14.656	14.656	−2.92	202.6
00040305−6106367	4905632480654004608	−6.0	0.12	0.00	53.448	53.448	−0.07	15.7
00043646 + 4124062	384060304935385984	−13.7	1.01	0.01	−7.058	−7.058	−0.33	28.8
00045403 + 3524010	2876804519751163008	−91.5	1.06	0.02	9.525	9.525	−0.45	154.2

(This table is available in its entirety in machine-readable form.)

Astrometric Solution database (Lindegren et al. 2016) was combined with distances from Astraatmadja & Bailer-Jones (2016) to calculate the Cartesian Galactic positions (X_{Gal}, Y_{Gal}, and Z_{Gal}) and velocities (particularly V_T). For $V_T \geqslant 75$ km s^{-1}, the authors noticed a considerable increase in the fractions of metal-poor and VMP stars in their own validation sample of low-metallicity stars from RAVE DR5. However, the full potential of this approach was still not clear at the time, because (i) those targets were selected with prior information of their metallicities from RAVE's moderate-resolution ($R \sim 7500$) spectroscopy and (ii) the limited coverage and quality of Gaia DR1 data did not allow for a confident (with small errors) investigation of the majority of their studied stars. In P19, despite this knowledge, the better astrometry from Gaia DR2 was still not available at the time of observations, hence only a simple PM (plus V-band magnitude and reddening) cut was applied. In this work, we seek to explore more fully the influence of kinematic-based target selection in finding VMP and EMP stars, taking advantage of Gaia EDR3 PMs and V_{los}. The results of these analyses will be (and are being) employed in future (and ongoing) observational campaigns.

We have cross-matched both the Gemini and SOAR samples with Gaia EDR3 to acquire accurate V_{los}, parallaxes, and PMs (Table 4). These measured parameters have been converted to the Cartesian Galactic phase-space positions and velocities using the `Astropy` package (Astropy Collaboration et al. 2013, 2018). The assumed in-plane distance from the Sun to the Galactic center is $R_{\odot} = 8.2$ kpc (Bland-Hawthorn & Gerhard 2016), which is compatible with the findings of Gravity Collaboration et al. (2019, 2020). We recall that stars in the SOAR sample have been observed with prior knowledge of their kinematics, derived from Gaia DR2 data. For the Gemini sample, matches with Gaia EDR3 have been found for all but two stars (Section 2). Out of these, 1766/1787 (99%) have non-negative parallaxes. The distances have been calculated through the inversion of these parallaxes[15] after recalibration (+0.017 mas[16]; Lindegren et al. 2021a). For the purpose of our investigation, we have applied a relative error cut, keeping stars with `parallax_over_error` $\geqslant 1$ (see Lindegren et al. 2021b). Despite being very permissive in comparison to the recent literature, this uncertainty cut is consistent with P18 (such that our study can be directly compared to theirs) and has the objective of not removing too many candidates. However, we note that, thanks to the improved astrometry of Gaia EDR3 in comparison to DR2, only a handful of (∼80) stars in the full (Gemini+SOAR+P19) sample have `parallax_over_error` $\leqslant 5$ (or missing/negative values). Furthermore, ∼91% of all stars observed have `parallax_over_error` $\geqslant 10$, providing reliability to our kinematic/dynamical calculations.

5.1. Why V_{TAV}?

In this work, we build on the results presented by P18. One of the refinements that we have made is the introduction of the V_{TAV} quantity (Section 2.2), which demands either PMs or V_{los}, but makes use of their combination whenever both are available. With the goal of performing a comprehensive analysis, we have divided the Z_{Gal} versus velocity diagrams into four different regions, represented with distinct grayish and white colors in Figure 4. We find that high efficiencies of VMP and EMP detections are achieved even if only one velocity component is known. The ±0.5 kpc stripe at the center of all panels is motivated by the characteristic scale height of thin-disk stars around the Galactic plane (Recio-Blanco et al. 2014; Li et al. 2018a), which is also consistent with the analysis of P18. The separation at 100 km s^{-1} approximately marks the end of the metal-rich-dominated ([Fe/H] > −2.0) portion of the diagrams, and can be considered a velocity limit between thin-disk ($\lesssim$100 km s^{-1}) and thick-disk/halo populations. This separation can be visualized by observing the large concentrations of black dots in Figure 4.

Indeed, it is expected that higher values of velocity should yield greater fractions of genuine halo stars; see Koppelman et al. (2018) and Posti et al. (2018) for recent discussions. However, as is made clear below, the chosen boundaries already produce quite high success rates. The combination of these cuts at ±0.5 kpc and 100 km s^{-1} defines the various areas in Figure 4. Then, we calculate the fractions of stars showing [Fe/H] $\leqslant -2.0$ (f_{VMP}) in each of these regions. We take these fractions as representative of the efficiency of finding VMP stars in each different portion of the Z_{Gal} versus velocity diagrams for stars originally identified as possibly metal-poor on the basis of the B&B photometric selection.

In the top panel of Figure 4, only V_{los} is employed, in combination with Z_{Gal}, to explore the f_{VMP} in the P19 sample. Although high success rates already appear for $|Z|_{Gal} \geqslant 0.5$ kpc, the number of available candidates in the P19 sample is reduced to approximately half of its total. In the middle panel of Figure 4, the visualization of (Z_{Gal}, V_T) space is similar to its presentation in the figures of P18. We note that almost the entire P19 sample has suitable PMs and parallaxes from Gaia

[15] During the reviewing process of this paper, distances derived from a probabilistic approach have been made available by Bailer-Jones et al. (2021) for sources in Gaia EDR3. Since our sample is fairly local (∼80% within 4 kpc; Figure 1), the differences between those authors' calculated distances and the ones adopted here are negligible (>10% for only a couple of stars). In fact, even considering the full sample (up to ∼8 kpc), only ∼5% of the stars with `parallax_over_error` $\geqslant 5$ show differences >10% in their distance estimates.

[16] The parallax offset depends in a nonlinear, nontrivial way on the (G-band) magnitude and color ($G_{BP} - G_{RP}$) of the source. For simplicity, we adopt a global correction equal to the median of quasars' parallaxes in Gaia EDR3 (Lindegren et al. 2021a).

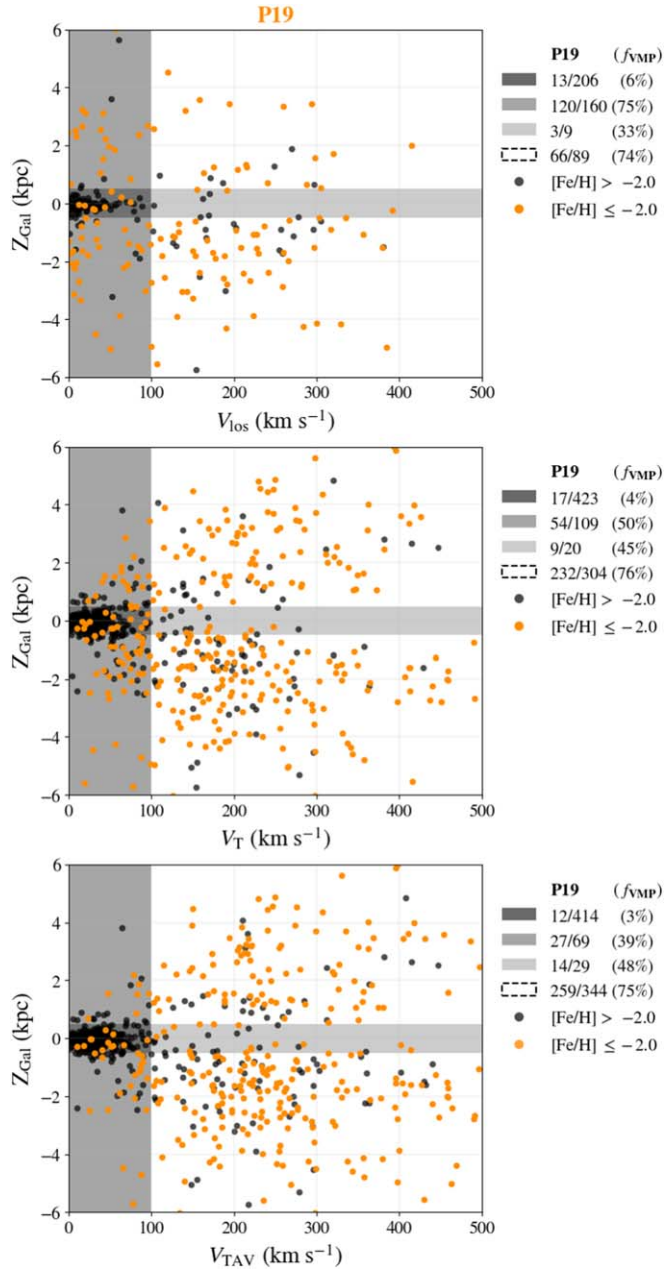

Figure 4. Diagrams of the P19 sample for Z_{Gal} vs. different components of velocity: V_{los} (top panel), V_T (middle), and V_{TAV} (bottom panel). To the right of each panel, the fractions of VMP stars for each gray-shaded and white regions are presented. Black and orange dots represent stars with [Fe/H] > −2.0 and VMP stars, respectively.

EDR3, allowing us to calculate accurate V_T for these stars. The f_{VMP} in the white regions of the (Z_{Gal}, V_T) diagram remains statistically the same as the (Z_{Gal}, V_{los}) one, but the number of stars has more than tripled, which is advantageous for planning an observational campaign.

The bottom panel of Figure 4 shows the Z_{Gal} versus V_{TAV} diagram for the P19 sample. Once more, the f_{VMP} in each area of the diagram is similar to previous panels, but there is an increase of ∼13% in the number of stars in the $|Z|_{Gal} \geqslant 0.5$ kpc and $V_{TAV} \geqslant 100$ km s^{-1} region, while maintaining high efficiency—almost double the f_{VMP} achieved by P19. This finding inspired the target-selection criteria for observations with Goodman/SOAR. Even though we had the prospect of improvements, these results were surprising because the B&B catalog is, by design, biased toward metal-poor stars. In general, from top to bottom, one can notice the increasing number of points in each diagram of Figure 4, but statistically equivalent success rates for the different regions are maintained, demonstrating the advantages of employing the V_{TAV} parameter.

5.2. Z_{Gal} versus V_{TAV} Diagrams and Final Success Rates

The individual impact of variations in $|Z|_{Gal}$ and V_{TAV} in the metallicity distribution function (MDF) of the full B&B sample are presented from the top and bottom rows of Figure 5, respectively. In the thin-disk-like regions ($|Z|_{Gal} < 0.5$ kpc and $V_{TAV} < 100$ km s^{-1}; left column), the MDFs peak at [Fe/H]∼ −0.7 and the f_{VMP} is only ∼5%. However, as we move to higher values of $|Z|_{Gal}$, the peak of the MDF is shifted to the VMP regime already at $|Z|_{Gal} > 0.5$ kpc (middle). The f_{VMP} reaches 86% for $|Z|_{Gal} > 3.0$ kpc (right), which reflects the lower metallicity of the Galactic halo in comparison to the canonical disk system, despite the already low-metallicity-biased B&B selection. For the V_{TAV} quantity, this smoother transition is noticeable from the extended MDF within the range $100 < V_{TAV}$ (km s^{-1}) < 150 (middle column). However, the f_{VMP} significantly increases at $V_{TAV} > 150$ km s^{-1} (right).

Figure 6 presents the Z_{Gal} versus V_{TAV} diagrams for the Gemini and SOAR samples. Colored symbols are VMP stars spectroscopically confirmed by the present work, following the same color scheme as Figures 1, 2, 3, and 5, while the black dots are those with [Fe/H] > − 2.0. The left panel shows the distributions of stars from Gemini and SOAR samples in this parameter space. Given the target selection described in Section 2.2, the majority of stars observed from SOAR occupy the most interesting regions of the Z_{Gal} versus V_{TAV} diagram. Interestingly, the few cases in which they are outside the VMP regions originate from differences between the Gaia DR2 and EDR3 parameters. The right panel presents the (Z_{Gal}, V_{TAV}) space of the full sample, including that from P19.

The f_{VMP} in each of the gray-shaded and white regions of the Z_{Gal} versus V_{TAV} diagrams are also provided in Figure 6. Table 5 lists the final success rates for each region and for various metallicity regimes ([Fe/H] $\leqslant -1.5$, $\leqslant -2.0$, $\leqslant -2.5$, and $\leqslant -3.0$), along with their respective $|Z|_{Gal}$ and V_{TAV} boundaries. These final efficiencies are drawn from the full sample for better statistics. Particularly in the white regions ($|Z|_{Gal} \geqslant 0.5$ kpc and $V_{TAV} \geqslant 100$ km s^{-1}), i.e., the thick disk/halo-like ones, the fractions of stars within [Fe/H]$\leqslant -1.5$, $\leqslant -2.0$, $\leqslant -2.5$, and $\leqslant -3.0$ are 96%, 76%, 28%, and 4%, respectively. Such effectiveness in the search for low-metallicity stars in the Galaxy is only rivaled by surveys with prior narrowband photometry at the wavelength of the Ca II K line (e.g., Youakim et al. 2017; Aguado et al. 2019; Da Costa et al. 2019). In the near future, we expect to be able to combine the astrometric information from Gaia's DRs with narrowband photometry from, e.g., S-PLUS (Southern-Photometric Local Universe Survey; Mendes de Oliveira et al. 2019), J-PLUS (Javalambre-Photometric Local Universe Survey; Cenarro et al. 2019), and J-PAS (Javalambre-Physics of the Accelerating Universe Astrophysical Survey; Bonoli et al. 2020), in order to obtain even better success rates, particularly in the EMP regime.

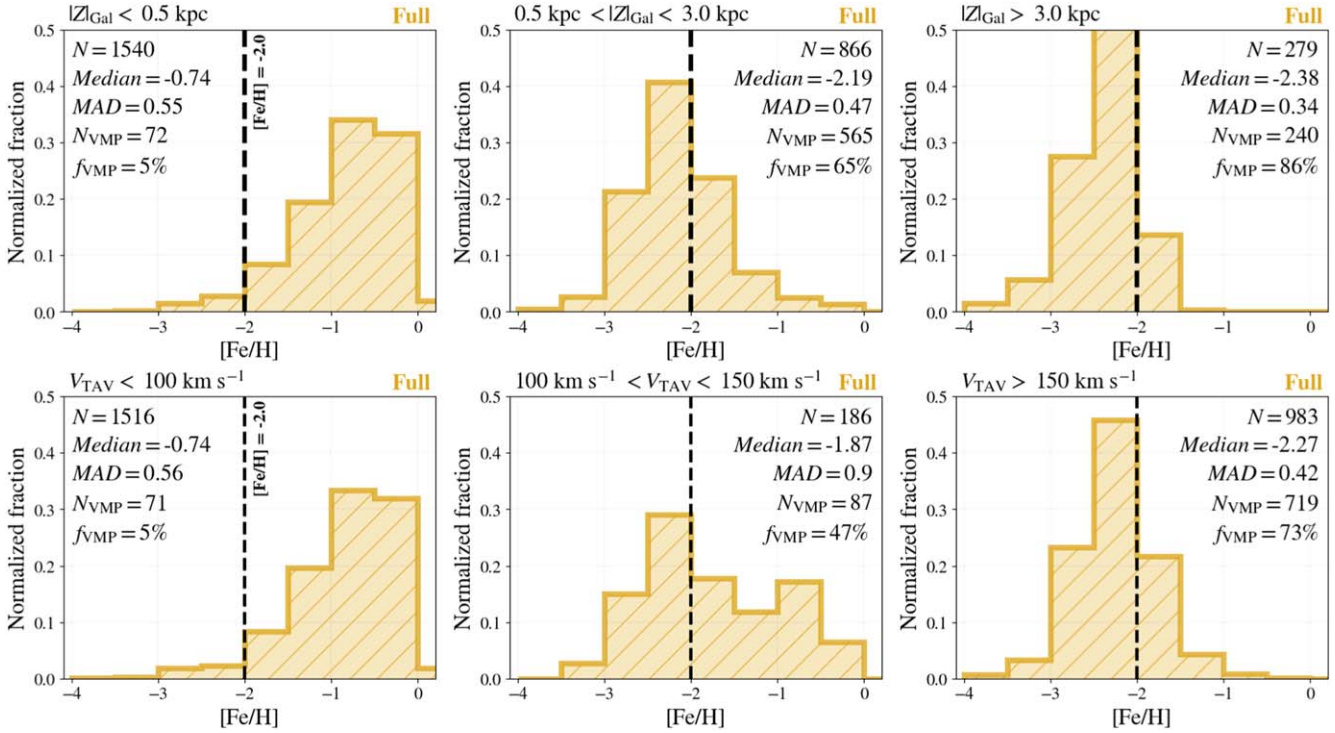

Figure 5. Metallicity distribution functions (MDFs) of stars observed from the B&B catalog. Histograms present the normalized fractions, and the total number of stars in each panel (N) is provided. Top panels show MDFs of the full (Gemini+SOAR+P19) sample for the slices: $|Z|_{\rm Gal} < 0.5$ kpc, $0.5 < |Z|_{\rm Gal}$ (kpc) < 3.0, and $|Z|_{\rm Gal} > 3.0$ kpc (left, middle, and right, respectively). Bottom panels show MDFs of the full sample, but for various ranges of $V_{\rm TAV}$: $V_{\rm TAV} < 100$ km s^{-1}, $100 < V_{\rm TAV}$ (km s^{-1}) < 150 and $V_{\rm TAV} > 150$ km s^{-1} (left, middle, and right, respectively). Median [Fe/H], median absolute deviation (MAD), total number ($N_{\rm VMP}$), and fraction of VMP stars ($f_{\rm VMP}$) are shown in each panel. Dashed vertical lines mark the VMP limit at [Fe/H] $= -2.0$, for reference.

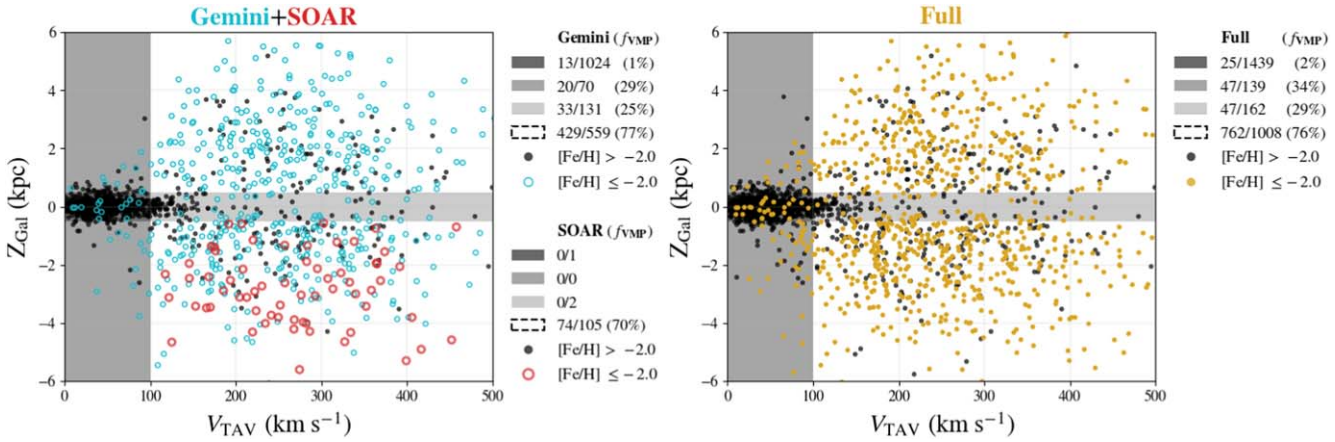

Figure 6. $Z_{\rm Gal}$ vs. $V_{\rm TAV}$ diagrams. Left: distribution of stars from Gemini (Section 2.1) and SOAR (Section 2.2) samples. Right: distribution of stars from the full (Gemini+SOAR+P19) sample. Colored symbols are VMP stars, while black ones have [Fe/H] > -2.0. Both panels are shown with a color scheme similar to those of Figures 1, 2, 3, and 5. Specific VMP fractions are also provided for each gray-shaded and white regions (see text and Table 5 for details) to the right of each panel.

Table 5
Regions of the $Z_{\rm Gal}$ vs. $V_{\rm TAV}$ Diagrams and Final Success Rates for Different Metallicities

Region (Color)	$\lvert Z\rvert_{\rm Gal}$ (kpc)	$V_{\rm TAV}$ (km s^{-1})	[Fe/H] $\leqslant -1.5$	[Fe/H] $\leqslant -2.0$	[Fe/H] $\leqslant -2.5$	[Fe/H] $\leqslant -3.0$
Dark gray	<0.5	<100	8^{+2}_{-1}%	2^{+1}_{-1}%	1^{+1}_{-0}%	0^{+0}_{-0}%
Medium gray	$\geqslant 0.5$	<100	58^{+8}_{-8}%	34^{+8}_{-7}%	17^{+7}_{-5}%	3^{+4}_{-2}%
Light gray	<0.5	$\geqslant 100$	52^{+8}_{-8}%	29^{+7}_{-6}%	9^{+6}_{-4}%	1^{+3}_{-1}%
White	$\geqslant 0.5$	$\geqslant 100$	96^{+1}_{-1}%	76^{+3}_{-3}%	28^{+3}_{-3}%	4^{+1}_{-1}%

5.3. Toomre Diagrams

For comparison, we have also investigated the success rates in finding low-metallicity stars using a kinematic-based target selection within different regions of the Toomre diagram (Figure 7). The peculiar motion of the Sun with respect to the local standard of rest (LSR) is $(U, V, W)_\odot = (11.10, 12.24, 7.25)$ km s^{-1} (Schönrich et al. 2010). The adopted velocity of the LSR is $V_{\rm LSR} = (0.0, 232.8, 0.0)$ km s^{-1} (McMillan 2017). Recently, purely acceleration-based estimates of the Galactic fundamental parameters have been made available, thanks to the direct measurement of the Solar System's acceleration from

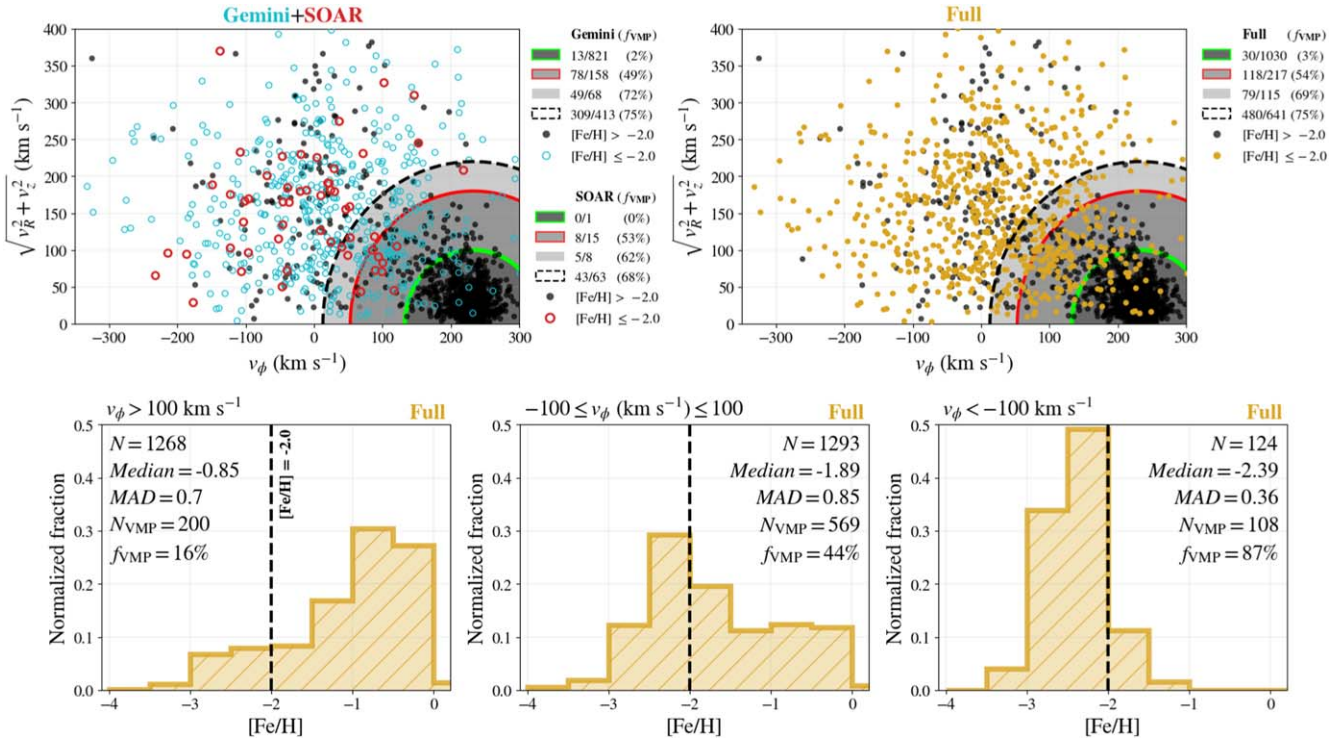

Figure 7. Top panels: Toomre diagrams ($\sqrt{v_R^2+v_z^2}$ vs. v_ϕ). Top left: Gemini (Section 2.1) and SOAR (Section 2.2) samples. Top right: full (Gemini+SOAR+P19) sample. Stars that are VMP are represented with colored symbols in the same color scheme used in Figures 1, 2, 3, 5, and 6. Black dots are stars with [Fe/H] > -2.0. Green and red solid lines mark the velocity boundaries for the thin ($|V_{\rm total} - V_{\rm LSR}| < 100$ km s^{-1}; dark gray) and thick disks (100 km s^{-1} $\leqslant |V_{\rm total} - V_{\rm LSR}| < 180$ km s^{-1}; medium gray), respectively (see text). Dashed line marks the transition region (180 km s^{-1} $\leqslant |V_{\rm total} - V_{\rm LSR}| < 220$ km s^{-1}; light gray stripe) between the thick disk and halo. Finally, the halo is defined by $|V_{\rm total} - V_{\rm LSR}| \geqslant 220$ km s^{-1} (white region). To the right of each panel, the specific VMP fractions ($f_{\rm VMP}$) in each of the described areas in ($\sqrt{v_R^2+v_z^2}$, v_ϕ) space are provided. Bottom panels: metallicity distribution functions (MDFs) of the full sample for various intervals of v_ϕ. Bottom left: $v_\phi > 100$ km s^{-1}. Bottom middle: $-100 \leqslant v_\phi$ (km s^{-1}) $\leqslant 100$. Bottom right: $v_\phi < -100$ km s^{-1}. Total numbers of stars (N), medians, median absolute deviations (MAD), numbers ($N_{\rm VMP}$), and fractions ($f_{\rm VMP}$) of VMP stars are also displayed in the corresponding panels. Dashed vertical lines mark the VMP limit at [Fe/H] $= -2.0$, for reference.

Gaia EDR3 astrometry. Nevertheless, the values adopted here have been chosen due to their consistency with the Galactic model of McMillan (2017), which will be employed for orbit integration in Section 5.4. Figure 7 shows the ($\sqrt{v_R^2+v_z^2}$, v_ϕ) space, where (v_R, v_ϕ, v_z) compose the velocity vector of each star in the cylindrical coordinate system (radial, azimuthal, and vertical directions, respectively). Stars in prograde motion have $v_\phi > 0$. Note that it is necessary to have measured $V_{\rm los}$ in order to calculate the complete set of (v_R, v_ϕ, v_z). This is a clear disadvantage in utilizing the Toomre diagram for selecting targets for systematic searches of low-metallicity stars, since many targets would be ignored due to lack of available $V_{\rm los}$. Therefore, we wish to evaluate whether or not the efficiency in finding VMP stars is hindered by the application of $Z_{\rm Gal}$ versus $V_{\rm TAV}$ diagram in comparison to $\sqrt{v_R^2+v_z^2}$ versus v_ϕ, where the complete phase-space vector needs to be available. In this context, we also study changes in the full sample's MDF with v_ϕ (see Figure 7).

For consistency with the analysis presented in Section 5.2, we have divided the Toomre diagrams into four regions, similar to what has been done for the ($Z_{\rm Gal}$, $V_{\rm TAV}$) space. In Figure 7, these are displayed in an arrangement similar to that used in Figure 6, with a gray scale tentatively representing different Galactic components. Stars that are VMP are shown with colored symbols in the same color scheme as Figures 1, 2, 3, 5, and 6. The dark gray area with a green contour contains stars within $|V_{\rm total} - V_{\rm LSR}| < 100$ km s^{-1}, where $V_{\rm total}$ is the complete velocity vector of a given star. This is the most crowded zone in both top panels of Figure 7, which is noticeable from the accumulation of black points around $v_\phi \sim V_{\rm LSR}$. This region in velocity space is representative of the thin disk (e.g., Venn et al. 2004; Bensby et al. 2014), and is also recognizable from its $f_{\rm VMP} \lesssim 3\%$ in both diagrams of Figure 7, despite the B&B selection. The predominance of this component is also perceptible from the MDF of stars with $v_\phi > 100$ km s^{-1} (bottom left panel of Figure 7). This MDF peaks at [Fe/H] ~ -0.8, but also shows an extended VMP tail associated with the thick disk and prograde portion of the halo.

Moving radially outward from the thin-disk region of the ($\sqrt{v_R^2+v_z^2}$, v_ϕ) space, the medium gray area between the green and red lines is defined by 100 km s^{-1} $\leqslant |V_{\rm total} - V_{\rm LSR}| < 180$ km s^{-1}, and is characteristic of the thick disk; for a recent discussion, see, e.g., Amarante et al. (2020b). A noteworthy feature of the Toomre diagrams in Figure 7 is the presence of high fractions ($\gtrsim$50%) of VMP stars in this thick-disk-like slice of the velocity space. We speculate that this feature is also due to the underlying B&B selection. This finding has led us to further scrutinize the presence of VMP and EMP stars associated with the Galactic disks, in Section 5.4.

The light gray stripe, defined by the dashed and red solid lines in Figure 7 (180 km s^{-1} $\leqslant |V_{\rm total} - V_{\rm LSR}| < 220$ km s^{-1}), comprises the tail of the velocity distribution of the Galactic disk (e.g., Bonaca et al. 2017; Koppelman et al. 2018). This transition region between thick disk and halo also contains stars

from the "splashed disk" (Belokurov et al. 2020; Amarante et al. 2020a; An & Beers 2020), considered to be the metal-rich, *in situ* counterpart of the halo (Bonaca et al. 2017, 2020; Haywood et al. 2018; Gallart et al. 2019; Di Matteo et al. 2019). The $f_{\rm VMP}$ in this area of the $(\sqrt{v_R^2+v_z^2}, v_\phi)$ space is statistically equivalent to the halo selection.

We note that the concentration of stars within $-50 \lesssim v_\phi$ (km s^{-1}) $\lesssim +50$, permeating all values of $\sqrt{v_R^2+v_z^2}$, is reminiscent of the Gaia-Sausage/Enceladus (GSE) merging event (Belokurov et al. 2018; Haywood et al. 2018; Helmi et al. 2018). However, considering v_ϕ alone, we also note the extended MDF shown in the bottom middle panel of Figure 7 ($-100 \leqslant v_\phi\,({\rm km\,s^{-1}}) \leqslant 100$), which peaks between $-2.5 < {\rm [Fe/H]} < -2.0$, but has a prominent metal-rich tail linked to the thick and splashed disks. On the other hand, the MDF in the $v_\phi < -100\,{\rm km\,s^{-1}}$ panel of Figure 7 (bottom right) is almost entirely comprised of VMP stars. These stars might also be associated with previously identified halo substructures, e.g., Sequoia (Myeong et al. 2019) and Thamnos (Koppelman et al. 2019). Indeed, independent efforts have suggested that these retrograde groups are more metal-poor than GSE (Matsuno et al. 2019; Dietz et al. 2020; Kordopatis et al. 2020; Monty et al. 2020). Nevertheless, these supposed remnants of now-destroyed dwarf galaxies are also of interest to this work, particularly because large numbers of VMP stars, including those exhibiting *r*-process-element enhancement (Gudin et al. 2021), have recently been demonstrated to be associated with them (Yuan et al. 2020; Limberg et al. 2021; see Section 5.4).

Finally, the black dashed line delineates the $|V_{\rm total} - V_{\rm LSR}| \geqslant 220\,{\rm km\,s^{-1}}$ zone of the Toomre diagrams. These are the white areas in both top panels of Figure 7. Stars inhabiting this part of the $(\sqrt{v_R^2+v_z^2}, v_\phi)$ space are from either the *in situ* or accreted components of the halo. The $f_{\rm VMP}$ of the full sample in this white region is similar to the one found for the halo-like portions of the $Z_{\rm Gal}$ versus $V_{\rm TAV}$ diagram in Section 5.2. Nonetheless, we have found no statistical differences in $f_{\rm VMP}$ between the prograde and retrograde components of the halo. To conclude, kinematic criteria based on the ($Z_{\rm Gal}$, $V_{\rm TAV}$) space can be as efficient as the traditional Toomre diagram in finding low-metallicity stars, with the additional advantage of not needing prior measurement of $V_{\rm los}$, thus enabling access to a larger number of candidates, while making optimal usage of this parameter whenever it is available. Therefore, we recommend consideration of the $V_{\rm TAV}$ quantity for the target selection of observational campaigns aiming to find VMP and EMP stars in the Galaxy.

5.4. Orbits of VMP/EMP Stars

We now examine the presence of dynamically interesting stars in all samples, which will become priority targets for high-resolution follow-up. First, we check for VMP and EMP stars residing in the kinematically defined thick disk (Section 5.3). In order to confirm whether or not these stars are truly confined to the disk system, we have used the publicly available library `AGAMA` (Vasiliev 2019) to integrate their orbits forward in time for ∼5 Gyr. The Galactic model employed is from McMillan (2017), and includes stellar and gaseous disks, a flattened bulge, and a spherical dark matter halo. The assumptions regarding the Galactic fundamental parameters are the same as in Sections 5 and 5.3. The $V_{\rm los}$ have been acquired from Gaia EDR3, where available, but we have only considered stars with `parallax_over_error` $\geqslant 5$ for this exercise. We have performed 1000 realizations of each star's orbit according to its uncertainties in the astrometric quantities, assuming Gaussian distributions for them. The medians of each dynamical parameter have been taken as our nominal values. Our investigation is focused on the maximum vertical distance achieved during a star's orbit ($Z_{\rm max}$), the perigalactic distance ($r_{\rm min}$), the apogalactic distance ($r_{\rm max}$), eccentricity ($e = (r_{\rm max} - r_{\rm min})/(r_{\rm max} + r_{\rm min})$), orbital energy ($E$), and the vertical component of angular momentum $L_z = R_{\rm Gal} \times v_\phi$, where $R_{\rm Gal} = \sqrt{X_{\rm Gal}^2 + Y_{\rm Gal}^2}$ is the plane-projected distance of a given star from the Galactic center.

The top panel of Figure 8 shows the distribution of the full sample in the $Z_{\rm max}$ versus $r_{\rm max}$ space. A star is considered to be on a planar orbit if its $Z_{\rm max} \leqslant 3$ kpc. The transition between the thick disk and halo is smooth in this diagram, as was previously observed in the full sample's MDFs for different slices of both $|Z|_{\rm Gal}$ (Figure 5) and v_ϕ (Figure 7). However, the $Z_{\rm max}$ limit at 3 kpc reflects the scale height of the thick disk recently estimated by Li & Zhao (2017). Crucially, it is also consistent with what has been considered in the analyses of Sestito et al. (2019, 2020). Interestingly, a separation between thick disk and halo at $Z_{\rm max} \sim 3$ kpc has also been achieved by Pérez-Villegas et al. (2020) in their independent analysis of orbits of Galactic globular clusters. We have paid particular attention to stars with ${\rm [Fe/H]} \leqslant -2.5$, as these are potential members of the aforementioned mono-enriched class (Hartwig et al. 2018). Hence, this metallicity cutoff is, apparently, more physically significant than the classic definitions of VMP and EMP stars, and is also consistent with the analyses of Sestito et al. (2020, 2021). For convenience, throughout this section, we refer to a star as "VMP/EMP" when ${\rm [Fe/H]} \leqslant -2.5$. A total of 275 stars in the full sample are consistent with this metallicity regime. These are shown as yellow dots in Figure 8, while those with ${\rm [Fe/H]} > -2.5$ are represented in gray. All VMP/EMP stars on planar orbits are plotted with red edges, and correspond to a fraction of $22^{+5}_{-4}\%$ (60/275), consistent with both Sestito et al. (2020) and Cordoni et al. (2021), despite our small biases toward halo kinematics (Section 2).

The bottom panel of Figure 8 presents the Toomre diagram for the full sample, divided according to the prescription above. One can see that there is a substantial number of VMP/EMP stars on low-$Z_{\rm max}$ orbits occupying the region of the $(\sqrt{v_R^2+v_z^2}, v_\phi)$ space characteristic of the thin and thick disks, as conjectured in Sections 5.2 and 5.3. These stars can be considered part of the third stellar population that resides in the Galactic disk, known as the metal-weak thick disk (MWTD; Norris et al. 1985; Morrison et al. 1990; Beers & Sommer-Larsen 1995; Bonifacio et al. 1999; Chiba & Beers 2000; Beers et al. 2002, 2014; Brown et al. 2008; Reddy & Lambert 2008; Kordopatis et al. 2013; Carollo et al. 2014, 2019; Hawkins et al. 2015; Li & Zhao 2017; Li et al. 2018a; An & Beers 2020; Di Matteo et al. 2020). Despite early suggestions that the MDF of the MWTD might extend down to the VMP/EMP regime (Beers & Sommer-Larsen 1995; Bonifacio et al. 1999), confirmation with large numbers of VMP/EMP stars was only possible thanks to the powerful combination of Gaia DR2 with large-scale spectroscopic surveys (e.g., LAMOST; Sestito et al. 2020). In fact, there is increasing evidence for the existence of an "ultra"-MWTD, reaching metallicities <-4.0 (Sestito et al. 2019; Di Matteo et al. 2020; Cordoni et al. 2021). A UMP star has even been found in the thin disk ($Z_{\rm max} < 0.5$ kpc; $e < 0.2$) (Schlaufman et al. 2018). On the other hand, about a third of

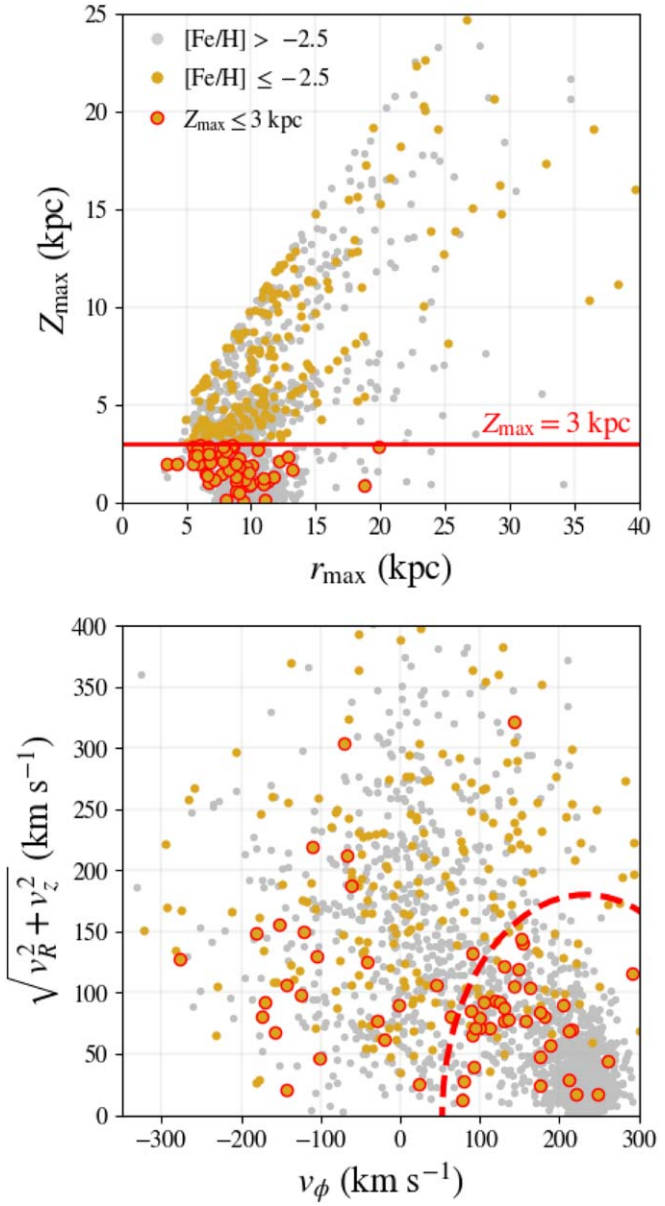

Figure 8. Top panel: $Z_{\rm max}$ vs. $r_{\rm max}$. Red horizontal line at $Z_{\rm max} = 3$ kpc marks the limit for stars considered to be on planar or halo-like orbits in our analysis (see text). Bottom panel: Toomre diagram, similar to Figure 7. Red dashed line marks the $|V_{\rm total} - V_{\rm LSR}| = 180$ km s^{-1} boundary between the thick disk and the transition region, as in Section 5.3. In both panels, gray dots represent stars with metallicities [Fe/H] > -2.5. Stars with [Fe/H] $\leqslant -2.5$ are displayed as yellow dots. Among these, the planar ones are plotted with red edges.

the planar VMP/EMP stars are rotating counter to the Galactic disks, some of them with $v_\phi \lesssim -100$ km s^{-1}).

The VMP/EMP stars on planar orbits are of crucial importance to constrain the early formation of the Galaxy. Recent cosmological zoom-in simulations have been pointing to the majority of VMP/EMP stars being born very early on ($z \gtrsim 5$), but mostly *ex situ*, in primordial galaxies that have been accreted by the main progenitor through hierarchical assembly up until $z \sim 1$ (Starkenburg et al. 2017a; El-Badry et al. 2018). Hence, these objects would be deposited into the main halo with a variety of different orbits, either prograde or retrograde (Sestito et al. 2021), and become phase-space mixed with those of *in situ* origin. However, given the presence of the ultra-MWTD, indistinguishable from the canonical thick disk from kinematics alone, Di Matteo et al. (2020) emphasize that the simplest deduction would be that these VMP/EMP stars were born in the Galaxy itself. Hence, these stars would have suffered from the same heating mechanism that operated to form both the splashed disk and the thick disk, i.e., the GSE event (Di Matteo et al. 2019; Gallart et al. 2019; Belokurov et al. 2020; Bonaca et al. 2020), although the exact role that merging events play in dynamical heating remains under debate (see, e.g., Jean-Baptiste et al. 2017; Amarante et al. 2020a). Nevertheless, these scenarios are not necessarily mutually exclusive, although the retrograde fraction of the VMP/EMP stars on planar orbits might be difficult to reconcile with the latter. In fact, Sestito et al. (2021) has noted that the Galaxy apparently hosts an excess of retrograde, low-$Z_{\rm max}$, low-metallicity stars in comparison to their simulations. The authors have further suggested that this aspect might be intrinsically related to a Milky Way–specific evolution, particularly the accretion of GSE's progenitor system. Such features of VMP/EMP stars on planar orbits in the Galaxy, especially the prograde/retrograde ratio, might help us understand this puzzling assembly history.

We continue our exploration for dynamically interesting stars in Figure 9, where the E versus L_z diagram is presented (top panel). This parameter space has been extensively utilized in the search for substructures in the Galaxy—especially in the halo—by, e.g., Chiba & Beers (2000) and numerous subsequent authors. For a recent review, see Helmi (2020). Unsurprisingly, we notice the spread of these objects on planar orbits throughout the locus, in (E, L_z) space, associated with either the disks or the low-E ($\lesssim -1.6 \times 10^5$ km^2 s^{-2}), retrograde halo. Curiously, the latter is also commonly attributed to the remnant of the proposed Thamnos event (Koppelman et al. 2019). Indeed, we had already noticed that VMP stars from this substructure are unequivocally contained within $Z_{\rm max} \lesssim 3.5$ kpc in Limberg et al. (2021). One might even speculate that the accretion of a small system like the Thamnos progenitor could have been the responsible for the apparent excess of retrograde low-$Z_{\rm max}$ stars reported by Sestito et al. (2021). However, this should be taken with caution, since both the specific chemical profile of this substructure (Monty et al. 2020), as well as its independence from GSE (Kordopatis et al. 2020), are still under active study (see also discussions about the consequences of massive mergers in Jean-Baptiste et al. (2017) and Koppelman et al. (2020)).

From the (E, L_z) space, we have also tentatively isolated stars from both GSE and Sequoia debris. We have placed characteristic selection boxes for each of these substructures (blue and green lines, respectively, in the top panel of Figure 9), using an approach similar both to that of Matsuno et al. (2019), who analyzed the MDFs and α-to-iron ratios of their member stars, as well to that of Massari et al. (2019), who studied possible dynamical associations between globular clusters and various Galactic components. For reference, we have also located the ω Centauri globular cluster in (E, L_z) space, which has been proposed to be the remnant nuclear star cluster of GSE (Pfeffer et al. 2021). The GSE selection is: $-1.7 \leqslant E\ (\times 10^5\ {\rm km^2\ s^{-2}}) \leqslant -1.2$, and $-0.5 \leqslant L_z\ (\times 10^3\ {\rm kpc\ km\ s^{-1}}) \leqslant +0.5$. For Sequoia: $-1.4 \leqslant E\ (\times 10^5\ {\rm km^2\ s^{-2}}) \leqslant -1.0$, and $L_z \leqslant -1.0 \times 10^3$ kpc km s^{-1}. The MDFs resulting from these cuts are presented in the bottom panel of Figure 9, with the same colors as their respective selection boxes. For comparison, we have also plotted the MDFs for the full sample (gray) and for those stars on planar orbits (red). The MDFs from both GSE and Sequoia mostly occupy the metallicity range of $-3.0 <$ [Fe/H] < -1.5,

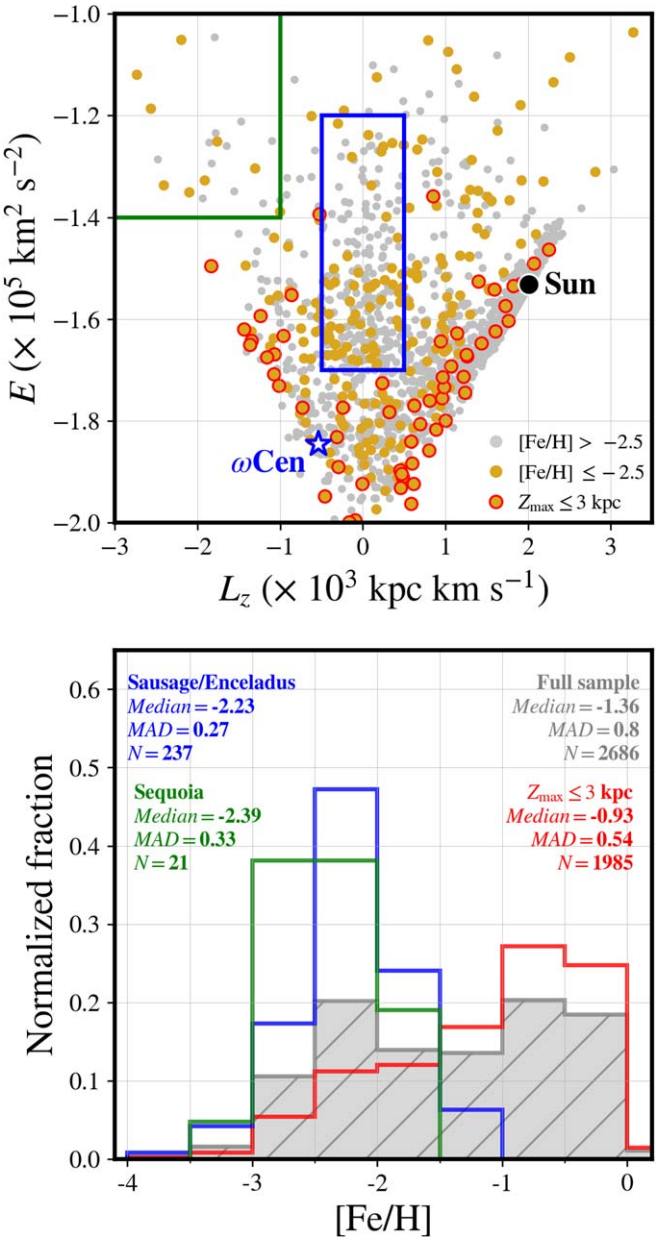

Figure 9. Top panel: E vs. L_z. Position of the Sun is indicated with a black circle: $(E, L_z)_\odot = (-1.5 \times 10^5$ km^2 s^{-2}, $+2.0 \times 10^3$ kpc km s$^{-1})$. Blue solid lines delineate our selection box for Gaia-Sausage/Enceladus (GSE; see text) stars. Blue star shows the position of the ω Centauri globular cluster: $(E, L_z)_{\omega\mathrm{Cen}} = (-1.8 \times 10^5$ km^2 s^{-2}, -0.5×10^3 kpc km s$^{-1})$. Green box represents the selection of Sequoia stars (see text). Gray dots represent stars with [Fe/H] > -2.5. Stars with [Fe/H] $\leqslant -2.5$ are displayed as yellow dots. Among these, the disk-like stars are plotted with red edges. Bottom panel: Metallicity distribution functions of the full (gray), the planar (red), GSE (blue), and Sequoia (green) samples. Medians, median absolute deviations (MAD), and total numbers of stars (N) are also shown.

with medians of [Fe/H] ~ -2.2 and ~ -2.4, respectively, but median absolute deviations that make them compatible with each other. Despite some overlap, these are much more metal-poor than the typical values found for both of these substructures in the literature, e.g., Helmi et al. (2018), Conroy et al. (2019a), Vincenzo et al. (2019), Amarante et al. (2020b), and Feuillet et al. (2020) for GSE; and Myeong et al. (2019), Matsuno et al. (2019), Monty et al. (2020), and Dietz et al. (2020) for Sequoia. We have experimented with other selections in velocity space, as recommended by Feuillet et al. (2020), but the results are equivalent. We conclude that this low-metallicity bias is an effect of the underlying B&B selection.

From the bottom panel of Figure 9, we note that the MDF of GSE is reminiscent of those presented in Figure 5 (for $|Z|_{\mathrm{Gal}} > 3$ kpc and $V_{\mathrm{TAV}} > 150$ km s^{-1}), commensurate with this substructure being the predominant population in the nearby, accreted halo. The presence of this component is also noticeable from the behavior of the full sample's MDF (Figure 9), which has two peaks, with the lowest-metallicity one being in the same location as GSE's ($-2.5 \leqslant$ [Fe/H] $\leqslant -2.0$). The other peak, at $-1.0 \leqslant$ [Fe/H] $\leqslant -0.5$, is associated with metal-rich, thin-disk stars, mistakenly selected as VMP candidates and followed up during our program. We note, however, the extended low-metallicity tail of the MDF representing the low-Z_{max} portion of the full sample, related to the previously discussed VMP/EMP stars with thick-disk-like kinematics.

Finally, we stress that not only the VMP/EMP stars with $Z_{\mathrm{max}} > 3$ kpc, but also those confined to the Galactic plane, exhibit a wide variety of orbital behaviors, as seen in Figures 8 and 9. Both of these populations span the full range of orbital e, a feature highlighted by Cordoni et al. (2021) in their analysis: they go from the very low ($e < 0.2$) values associated with disk-like features, to the very high ($e > 0.8$) values typical of GSE debris. The mild-e ($0.4 < e < 0.6$) stars might also be associated with substructures of *ex situ* nature (see Helmi 2020), but most of them apparently belong to the *in situ* counterpart of the halo. Cordoni et al. (2021) highlights that VMP/EMP stars presenting low-to-mild-e, low-Z_{max} orbits follow the e distributions of simulated thick disks constructed via heating mechanisms by Sales et al. (2009). The retrograde counterpart of such a population would likely be an accreted one, according to those authors. This presented "continuity" (in the words of Di Matteo et al. (2020)) in the dynamical properties of the most metal-poor stars will certainly need to be taken into consideration in future simulation efforts trying to reproduce the birth and evolution of the Milky Way.

6. Conclusions

In this paper, we have presented a low-resolution ($R \sim 2000$) spectroscopic study of 1897 metal-poor star candidates selected in the Best & Brightest Survey (Schlaufman & Casey 2014). The observations have been conducted with either the GMOS/Gemini (North and South) or Goodman/SOAR combinations between semesters 2014A and 2019B. We have obtained the atmospheric parameters (T_{eff}, $\log g$, and [Fe/H]) for these stars, as well as carbon and magnesium abundance ratios for most of them. Furthermore, we have utilized the phase-space information provided by Gaia EDR3 to perform an in-depth investigation on the influence of kinematic-based target selection criteria in the efficiency of finding VMP stars. Finally, we have explored the presence of dynamically interesting VMP/EMP stars in our sample. Our main results can be summarized as follows.

1. Overall, 56% (1064) of the newly observed stars have [Fe/H] < -1.0, 30% (566) are VMP, and 2% (35) are EMP. Combined with the previously published data of P19, the full B&B sample is now one of the largest homogeneously analyzed compilations of bright ($V \lesssim 14$) VMP and EMP stars available.

2. There are 191 CEMP stars in the Gemini+SOAR sample, 94 from Group I and 97 from Group II in the Yoon-Beers A(C)−[Fe/H] diagram.
3. The fraction of CEMP stars increases with decreasing metallicity. In the VMP and EMP regimes, we have found 19% and 43%, respectively.
4. We have introduced the $V_{\rm TAV}$ quantity, which demands either PMs or $V_{\rm los}$, but makes optimal use of their combination when both are available. We have explored the $Z_{\rm Gal}$ versus $V_{\rm TAV}$ diagrams, and confirmed that the $f_{\rm VMP}$ grows for greater distances from the Galactic plane and velocities within the full B&B sample.
5. The final success rates that have been achieved for $Z_{\rm Gal} \geqslant 0.5$ kpc and $V_{\rm TAV} \geqslant 100\,{\rm km\,s^{-1}}$ are 96%, 76%, 28%, and 4% for [Fe/H] $\leqslant -1.5$, $\leqslant -2.0$, $\leqslant -2.5$, and $\leqslant -3.0$, respectively.
6. Using the Toomre diagram, the $f_{\rm VMP}$ in the kinematically defined halo is equivalent (at the 1σ level) to what has been found for the most interesting regions of the ($Z_{\rm Gal}$, $V_{\rm TAV}$) space.
7. After integrating their orbits, 22% of the stars with [Fe/H] $\leqslant -2.5$ have been found to be confined within $Z_{\rm max} \leqslant 3$ kpc. However, the VMP/EMP stars vetted here exhibit a wide variety of orbital behaviors, spanning all values of L_z and orbital eccentricity, in keeping with the post-Gaia literature.
8. Most of the VMP/EMP stars on planar orbits can be kinematically ($100\,{\rm km\,s^{-1}} \leqslant |V_{\rm total} - V_{\rm LSR}| < 180\ {\rm km\,s^{-1}}$) and dynamically ($e \lesssim 0.6$) attributed to the Galactic metal-weak thick disk. Moreover, a third of these planar, mild-e stars are retrograde (some with $v_\phi \lesssim -100\,{\rm km\,s^{-1}}$), and their origin remains unclear.
9. Stars on halo-like orbits ($Z_{\rm max} > 3$ kpc) with $e \gtrsim 0.8$ are generally associated with the GSE merging event. On the other hand, those with mild values of e might be linked to either the *in situ* counterpart of the halo or other accreted substructures (e.g., Sequoia).

We note that there remain many thousands of candidate metal-poor stars originally identified in the B&B survey, as well as in the HK and Hamburg/ESO surveys, which have not yet been vetted with low-resolution spectroscopy. Given the high success rates for the identification of VMP stars demonstrated by our kinematic-selection approach, it is feasible to go directly to high-resolution follow-up for many of these stars in future campaigns.

The authors thank Angeles Prez-Villegas for insightful discussions at the early stages of this work. We also thank the anonymous referee for a useful report. G.L. acknowledges CAPES (PROEX; Proc. 88887.481172/2020-00) and CNPq (PIBIC; Proc. 144638/2018-5). R.M.S. acknowledges CNPq (Proc. 436696/2018-5 and 306667/2020-7). S.R. would like to acknowledge support from FAPESP (Proc. 2015/50374-0 and 2014/18100-4), CAPES, and CNPq. H.D.P. thanks FAPESP Proc. 2018/21250-9. D.S., V.M.P., and T.C.B. acknowledge partial support from grant PHY 14-30152, Physics Frontier Center/JINA Center for the Evolution of the Elements (JINA-CEE), awarded by the US National Science Foundation. The work of V.M.P. is supported by NOIRLab, which is managed by the Association of Universities for Research in Astronomy (AURA) under a cooperative agreement with the National Science Foundation. Y.S.L. acknowledges support from a National Research Foundation (NRF) of Korea grant funded by the Ministry of Science and ICT (NRF-2018R1A2B6003961).

This work is partially based on observations obtained under programs SO-2018B-010 and SO-2019B-013 at the Southern Astrophysical Research (SOAR) telescope, which is a joint project of the Ministério da Ciência, Tecnologia e Inovações (MCTI/LNA) do Brasil, the US National Science Foundations NOIRLab, the University of North Carolina at Chapel Hill (UNC), and Michigan State University (MSU). This research is also partially based on observations obtained under programs GN-2015A-Q-76, GN-2015B-Q-86, GN-2016A-DD-3, GN-2016A-Q-75, GN-2016B-Q-77, GN-2017A-Q-82, GN-2017B-Q-75, GN-2017B-Q-79, GN-2018A-Q-403, GN-2018B-Q-316, GN-2019A-Q-309, GN-2019B-Q-403, GS-2014A-Q-74, GS-2014A-Q-8, GS-2015A-Q-77, GS-2015A-Q-92, GS-2015B-Q-71, GS-2016A-Q-76, GS-2016B-Q-81, GS-2017A-Q-86, GS-2017B-Q-75, GS-2017B-Q-84, GS-2018A-Q-406, and GS-2018B-Q-315 at the international Gemini Observatory, a program of NSF's NOIRLab, which is managed by the Association of Universities for Research in Astronomy (AURA) under a cooperative agreement with the National Science Foundation, on behalf of the Gemini Observatory partnership: the National Science Foundation (United States), National Research Council (Canada), Agencia Nacional de Investigación y Desarrollo (Chile), Ministerio de Ciencia, Tecnología e Innovación (Argentina), Ministério da Ciência, Tecnologia e Inovações (Brazil), and the Korea Astronomy and Space Science Institute (Republic of Korea).

This work has made use of data from the European Space Agency (ESA) mission Gaia (https://www.cosmos.esa.int/gaia), processed by the Gaia Data Processing and Analysis Consortium (DPAC, https://www.cosmos.esa.int/web/gaia/dpac/consortium. Funding for the DPAC has been provided by national institutions, in particular the institutions participating in the Gaia Multilateral Agreement. This research has made use of the SIMBAD database and VizieR catalog access tool, operated at CDS, Strasbourg, France. This research was made possible through the use of the AAVSO Photometric All-Sky Survey (APASS), funded by the Robert Martin Ayers Sciences Fund and NSF AST-1412587. This publication makes use of data products from the Two Micron All Sky Survey, which is a joint project of the University of Massachusetts and the Infrared Processing and Analysis Center/California Institute of Technology, funded by the National Aeronautics and Space Administration and the National Science Foundation.

This research has been conducted despite the ongoing dismantling of the Brazilian scientific system.

Facilities: Gemini North (8.1 m): GMOS-N, Gemini South (8.1 m): GMOS-S, SOAR (4.1 m): Goodman.

Software: `matplotlib` (Hunter 2007), `Numpy` (van der Walt et al. 2011), `scipy` (Virtanen et al. 2020).

ORCID iDs

Guilherme Limberg https://orcid.org/0000-0002-9269-8287
Rafael M. Santucci https://orcid.org/0000-0002-7529-1442
Silvia Rossi https://orcid.org/0000-0001-7479-5756
Derek Shank https://orcid.org/0000-0001-9723-6121
Vinicius M. Placco https://orcid.org/0000-0003-4479-1265
Timothy C. Beers https://orcid.org/0000-0003-4573-6233
Kevin C. Schlaufman https://orcid.org/0000-0001-5761-6779
Andrew R. Casey https://orcid.org/0000-0003-0174-0564
Young Sun Lee https://orcid.org/0000-0001-5297-4518

References

Abbott, B. P., Abbott, R., Abbott, T. D., et al. 2017a, ApJL, 848, L12
Abbott, B. P., Abbott, R., Abbott, T. D., et al. 2017b, ApJL, 848, L13
Abbott, B. P., Abbott, R., Abbott, T. D., et al. 2017c, PhRvL, 119, 161101
Aguado, D. S., González Hernández, J. I., Allende Prieto, C., & Rebolo, R. 2018, ApJL, 852, L20
Aguado, D. S., Youakim, K., González Hernández, J. I., et al. 2019, MNRAS, 490, 2241
Allen, D. M., Ryan, S. G., Rossi, S., Beers, T. C., & Tsangarides, S. A. 2012, A&A, 548, A34
Amarante, J. A. S., Beraldo e Silva, L., Debattista, V. P., & Smith, M. C. 2020a, ApJL, 891, L30
Amarante, J. A. S., Smith, M. C., & Boeche, C. 2020b, MNRAS, 492, 3816
An, D., & Beers, T. C. 2020, ApJ, 897, 39
Aoki, W., Beers, T. C., Christlieb, N., et al. 2007, ApJ, 655, 492
Aoki, W., Norris, J. E., Ryan, S. G., Beers, T. C., & Ando, H. 2002, ApJ, 567, 1166
Arcavi, I., Hosseinzadeh, G., Howell, D. A., et al. 2017, Natur, 551, 64
Asplund, M., Grevesse, N., Sauval, A. J., & Scott, P. 2009, ARA&A, 47, 481
Astraatmadja, T. L., & Bailer-Jones, C. A. L. 2016, ApJ, 833, 119
Astropy Collaboration, Price-Whelan, A. M., Sipőcz, B. M., et al. 2018, AJ, 156, 123
Astropy Collaboration, Robitaille, T. P., Tollerud, E. J., et al. 2013, A&A, 558, A33
Bailer-Jones, C. A. L., Rybizki, J., Fouesneau, M., Demleitner, M., & Andrae, R. 2021, AJ, 161, 147
Banerjee, P., Wu, M.-R., & Yuan, Z. 2020, ApJL, 902, L34
Beers, T. C., Carollo, D., Ivezić, Ž., et al. 2012, ApJ, 746, 34
Beers, T. C., & Christlieb, N. 2005, ARA&A, 43, 531
Beers, T. C., Drilling, J. S., Rossi, S., et al. 2002, AJ, 124, 931
Beers, T. C., Norris, J. E., Placco, V. M., et al. 2014, ApJ, 794, 58
Beers, T. C., Placco, V. M., Carollo, D., et al. 2017, ApJ, 835, 81
Beers, T. C., Preston, G. W., & Shectman, S. A. 1985, AJ, 90, 2089
Beers, T. C., Preston, G. W., & Shectman, S. A. 1992, AJ, 103, 1987
Beers, T. C., & Sommer-Larsen, J. 1995, ApJS, 96, 175
Belczynski, K., Askar, A., Arca-Sedda, M., et al. 2018, A&A, 615, A91
Belokurov, V., Erkal, D., Evans, N. W., Koposov, S. E., & Deason, A. J. 2018, MNRAS, 478, 611
Belokurov, V., Sanders, J. L., Fattahi, A., et al. 2020, MNRAS, 494, 3880
Bensby, T., Feltzing, S., & Oey, M. S. 2014, A&A, 562, A71
Bidelman, W. P., & MacConnell, D. J. 1973, AJ, 78, 687
Bisterzo, S., Gallino, R., Straniero, O., Cristallo, S., & Käppeler, F. 2011, MNRAS, 418, 284
Bland-Hawthorn, J., & Gerhard, O. 2016, ARA&A, 54, 529
Bonaca, A., Conroy, C., Cargile, P. A., et al. 2020, ApJL, 897, L18
Bonaca, A., Conroy, C., Wetzel, A., Hopkins, P. F., & Kereš, D. 2017, ApJ, 845, 101
Bond, H. E. 1970, ApJS, 22, 117
Bond, H. E. 1980, ApJS, 44, 517
Bonifacio, P., Caffau, E., Spite, M., et al. 2015, A&A, 579, A28
Bonifacio, P., Centurion, M., & Molaro, P. 1999, MNRAS, 309, 533
Bonoli, S., Marín-Franch, A., Varela, J., et al. 2020, arXiv:2007.01910
Brown, W. R., Beers, T. C., Wilhelm, R., et al. 2008, AJ, 135, 564
Burbidge, E. M., Burbidge, G. R., Fowler, W. A., & Hoyle, F. 1957, RvMP, 29, 547
Cameron, A. G. W. 1957, PASP, 69, 201
Carollo, D., Beers, T. C., Bovy, J., et al. 2012, ApJ, 744, 195
Carollo, D., Beers, T. C., Chiba, M., et al. 2010, ApJ, 712, 692
Carollo, D., Beers, T. C., Lee, Y. S., et al. 2007, Natur, 450, 1020
Carollo, D., Chiba, M., Ishigaki, M., et al. 2019, ApJ, 887, 22
Carollo, D., Freeman, K., Beers, T., et al. 2014, ApJ, 788, 180
Casey, A. R., & Schlaufman, K. C. 2015, ApJ, 809, 110
Cayrel, R., Depagne, E., Spite, M., et al. 2004, A&A, 416, 1117
Cenarro, A. J., Moles, M., Cristóbal-Hornillos, D., et al. 2019, A&A, 622, A176
Charbonnel, C. 1995, ApJL, 453, L41
Chiappini, C., Matteucci, F., & Gratton, R. 1997, ApJ, 477, 765
Chiba, M., & Beers, T. C. 2000, AJ, 119, 2843
Choi, J., Dotter, A., Conroy, C., et al. 2016, ApJ, 823, 102
Christlieb, N. 2003, RvMA, 16, 191
Christlieb, N., Schörck, T., Frebel, A., et al. 2008, A&A, 484, 721
Clemens, J. C., Crain, J. A., & Anderson, R. 2004, Proc. SPIE, 5492, 331
Cohen, J. G., Christlieb, N., McWilliam, A., et al. 2008, ApJ, 672, 320
Conroy, C., Bonaca, A., Cargile, P., et al. 2019b, ApJ, 883, 107
Conroy, C., Naidu, R. P., Zaritsky, D., et al. 2019a, ApJ, 887, 237
Cordoni, G., Da Costa, G. S., Yong, D., et al. 2021, MNRAS, 503, 2539
Côté, B., Eichler, M., Arcones, A., et al. 2019, ApJ, 875, 106
Côté, B., Fryer, C. L., Belczynski, K., et al. 2018, ApJ, 855, 99
Cruz, M. A., Cogo-Moreira, H., & Rossi, S. 2018, MNRAS, 475, 4781
Cui, X.-Q., Zhao, Y.-H., Chu, Y.-Q., et al. 2012, RAA, 12, 1197
Da Costa, G. S., Bessell, M. S., Mackey, A. D., et al. 2019, MNRAS, 489, 5900
Dalton, G., Trager, S. C., Abrams, D. C., et al. 2012, Proc. SPIE, 8446, 84460P
Davies, R. L., Allington-Smith, J. R., Bettess, P., et al. 1997, Proc. SPIE, 2871, 1099
de Jong, R. S., Barden, S., Bellido-Tirado, O., et al. 2014, Proc. SPIE, 9147, 91470M
de Jong, R. S., Bellido-Tirado, O., Chiappini, C., et al. 2012, Proc. SPIE, 8446, 84460T
Di Matteo, P., Haywood, M., Lehnert, M. D., et al. 2019, A&A, 632, A4
Di Matteo, P., Spite, M., Haywood, M., et al. 2020, A&A, 636, A115
Dietz, S. E., Yoon, J., Beers, T. C., & Placco, V. M. 2020, ApJ, 894, 34
Dotter, A. 2016, ApJS, 222, 8
Drout, M. R., Piro, A. L., Shappee, B. J., et al. 2017, Sci, 358, 1570
Dvorkin, I., Daigne, F., Goriely, S., Vangioni, E., & Silk, J. 2020, arXiv:2010.00625
El-Badry, K., Bland-Hawthorn, J., Wetzel, A., et al. 2018, MNRAS, 480, 652
Ezzeddine, R., Frebel, A., Roederer, I. U., et al. 2019, ApJ, 876, 97
Ezzeddine, R., Rasmussen, K., Frebel, A., et al. 2020, ApJ, 898, 150
Feuillet, D. K., Feltzing, S., Sahlholdt, C. L., & Casagrande, L. 2020, MNRAS, 497, 109
Frebel, A. 2018, ARNPS, 68, 237
Frebel, A., Chiti, A., Ji, A. P., Jacobson, H. R., & Placco, V. M. 2015, ApJL, 810, L27
Frebel, A., Christlieb, N., Norris, J. E., et al. 2006, ApJ, 652, 1585
Frebel, A., & Norris, J. E. 2015, ARA&A, 53, 631
Gaia Collaboration, Brown, A. G. A., Vallenari, A., et al. 2016b, A&A, 595, A2
Gaia Collaboration, Brown, A. G. A., Vallenari, A., et al. 2018, A&A, 616, A1
Gaia Collaboration, Brown, A. G. A., Vallenari, A., et al. 2021, A&A, 649, A1
Gaia Collaboration, Prusti, T., de Bruijne, J. H. J., et al. 2016a, A&A, 595, A1
Gallart, C., Bernard, E. J., Brook, C. B., et al. 2019, NatAs, 3, 932
Gimeno, G., Roth, K., Chiboucas, K., et al. 2016, Proc. SPIE, 9908, 99082S
Gravity Collaboration, Abuter, R., & Amorim, A. 2019, A&A, 625, L10
Gravity Collaboration, Abuter, R., & Amorim, A. 2020, A&A, 636, L5
Gudin, D., Shank, D., Beers, T. C., et al. 2021, ApJ, 908, 79
Hansen, T., Hansen, C. J., Christlieb, N., et al. 2015, ApJ, 807, 173
Hansen, T. T., Andersen, J., Nordström, B., et al. 2016, A&A, 588, A3
Hansen, T. T., Holmbeck, E. M., Beers, T. C., et al. 2018, ApJ, 858, 92
Hartwig, T., Yoshida, N., Magg, M., et al. 2018, MNRAS, 478, 1795
Hawkins, K., Jofré, P., Masseron, T., & Gilmore, G. 2015, MNRAS, 453, 758
Haynes, C. J., & Kobayashi, C. 2019, MNRAS, 483, 5123
Haywood, M., Di Matteo, P., Lehnert, M. D., et al. 2018, ApJ, 863, 113
Heger, A., & Woosley, S. E. 2010, ApJ, 724, 341
Helmi, A. 2020, ARA&A, 58, 205
Helmi, A., Babusiaux, C., Koppelman, H. H., et al. 2018, Natur, 563, 85
Henden, A., & Munari, U. 2014, CoSka, 43, 518
Herwig, F. 2005, ARA&A, 43, 435
Hill, V., Plez, B., Cayrel, R., et al. 2002, A&A, 387, 560
Holmbeck, E. M., Hansen, T. T., Beers, T. C., et al. 2020, ApJS, 249, 30
Hunter, J. D. 2007, CSE, 9, 90
Ito, H., Aoki, W., Beers, T. C., et al. 2013, ApJ, 773, 33
Jean-Baptiste, I., Di Matteo, P., Haywood, M., et al. 2017, A&A, 604, A106
Ji, A. P., Drout, M. R., & Hansen, T. T. 2019, ApJ, 882, 40
Ji, A. P., & Frebel, A. 2018, ApJ, 856, 138
Keller, S. C., Bessell, M. S., Frebel, A., et al. 2014, Natur, 506, 463
Kobayashi, C., Karakas, A. I., & Lugaro, M. 2020, ApJ, 900, 179
Kollmeier, J. A., Zasowski, G., Rix, H.-W., et al. 2017, arXiv:1711.03234
Koppelman, H., Helmi, A., & Veljanoski, J. 2018, ApJL, 860, L11
Koppelman, H. H., Bos, R. O. Y., & Helmi, A. 2020, A&A, 642, L18
Koppelman, H. H., Helmi, A., Massari, D., Price-Whelan, A. M., & Starkenburg, T. K. 2019, A&A, 631, L9
Kordopatis, G., Gilmore, G., Wyse, R. F. G., et al. 2013, MNRAS, 436, 3231
Kordopatis, G., Recio-Blanco, A., Schultheis, M., & Hill, V. 2020, A&A, 643, A69
Kunder, A., Kordopatis, G., Steinmetz, M., et al. 2017, AJ, 153, 75
Lattimer, J. M., & Schramm, D. N. 1974, ApJL, 192, L145
Lee, Y. S., Beers, T. C., Allende Prieto, C., et al. 2011, AJ, 141, 90
Lee, Y. S., Beers, T. C., Kim, Y. K., et al. 2017, ApJ, 836, 91
Lee, Y. S., Beers, T. C., & Kim, Y. K. 2019, ApJ, 885, 102
Lee, Y. S., Beers, T. C., Masseron, T., et al. 2013, AJ, 146, 132

Lee, Y. S., Beers, T. C., Sivarani, T., et al. 2008a, AJ, 136, 2022
Lee, Y. S., Beers, T. C., Sivarani, T., et al. 2008b, AJ, 136, 2050
Li, C., & Zhao, G. 2017, ApJ, 850, 25
Li, C., Zhao, G., Zhai, M., & Jia, Y. 2018a, ApJ, 860, 53
Li, H., Tan, K., & Zhao, G. 2018b, ApJS, 238, 16
Limberg, G., Rossi, S., Beers, T. C., et al. 2021, ApJ, 907, 10
Lindegren, L., Bastian, U., Biermann, M., et al. 2021a, A&A, 649, A4
Lindegren, L., Klioner, S. A., Hernández, J., et al. 2021b, A&A, 649, A2
Lindegren, L., Lammers, U., Bastian, U., et al. 2016, A&A, 595, A4
Lucatello, S., Beers, T. C., Christlieb, N., et al. 2006, ApJL, 652, L37
Lucatello, S., Tsangarides, S., Beers, T. C., et al. 2005, ApJ, 625, 825
Massari, D., Koppelman, H. H., & Helmi, A. 2019, A&A, 630, L4
Matsuno, T., Aoki, W., & Suda, T. 2019, ApJL, 874, L35
McMillan, P. J. 2017, MNRAS, 465, 76
Mendes de Oliveira, C., Ribeiro, T., Schoenell, W., et al. 2019, MNRAS, 489, 241
Monty, S., Venn, K. A., Lane, J. M. M., Lokhorst, D., & Yong, D. 2020, MNRAS, 497, 1236
Morrison, H. L., Flynn, C., & Freeman, K. C. 1990, AJ, 100, 1191
Myeong, G. C., Vasiliev, E., Iorio, G., Evans, N. W., & Belokurov, V. 2019, MNRAS, 488, 1235
Nomoto, K., Kobayashi, C., & Tominaga, N. 2013, ARA&A, 51, 457
Norris, J., Bessell, M. S., & Pickles, A. J. 1985, ApJS, 58, 463
Norris, J. E., Ryan, S. G., & Beers, T. C. 1996, ApJS, 107, 391
Norris, J. E., Ryan, S. G., & Beers, T. C. 1997, ApJ, 488, 350
Pérez-Villegas, A., Barbuy, B., Kerber, L. O., et al. 2020, MNRAS, 491, 3251
Pfeffer, J., Lardo, C., Bastian, N., Saracino, S., & Kamann, S. 2021, MNRAS, 500, 2514
Pian, E., D'Avanzo, P., Benetti, S., et al. 2017, Natur, 551, 67
Placco, V. M., Beers, T. C., Reggiani, H., & Meléndez, J. 2016a, ApJL, 829, L24
Placco, V. M., Beers, T. C., Santucci, R. M., et al. 2018, AJ, 155, 256
Placco, V. M., Frebel, A., Beers, T. C., et al. 2013, ApJ, 770, 104
Placco, V. M., Frebel, A., Beers, T. C., et al. 2014a, ApJ, 781, 40
Placco, V. M., Frebel, A., Beers, T. C., et al. 2016b, ApJ, 833, 21
Placco, V. M., Frebel, A., Beers, T. C., & Stancliffe, R. J. 2014b, ApJ, 797, 21
Placco, V. M., Santucci, R. M., Beers, T. C., et al. 2019, ApJ, 870, 122
Planck Collaboration, Ade, P. A. R., Aghanim, N., et al. 2016, A&A, 594, A13
Posti, L., Helmi, A., Veljanoski, J., & Breddels, M. A. 2018, A&A, 615, A70
Rasmussen, K. C., Zepeda, J., Beers, T. C., et al. 2020, ApJ, 905, 20
Recio-Blanco, A., de Laverny, P., Kordopatis, G., et al. 2014, A&A, 567, A5
Reddy, B. E., & Lambert, D. L. 2008, MNRAS, 391, 95
Reggiani, H., Meléndez, J., Kobayashi, C., Karakas, A., & Placco, V. 2017, A&A, 608, A46
Reggiani, H., Schlaufman, K. C., Casey, A. R., & Ji, A. P. 2020, AJ, 160, 173
Riello, M., De Angeli, F., Evans, D. W., et al. 2021, A&A, 649, A3
Roederer, I. U., Placco, V. M., & Beers, T. C. 2016, ApJL, 824, L19
Roederer, I. U., Preston, G. W., Thompson, I. B., et al. 2014, AJ, 147, 136
Rossi, S., Beers, T. C., & Sneden, C. 1999, in ASP Conf. Ser., 165, The Third Stromlo Symposium: The Galactic Halo, ed. B. K. Gibson, R. S. Axelrod, & M. E. Putman (San Francisco, CA: ASP), 264
Rossi, S., Beers, T. C., Sneden, C., et al. 2005, AJ, 130, 2804
Ryan, S. G., Aoki, W., Norris, J. E., & Beers, T. C. 2005, ApJ, 635, 349
Safarzadeh, M., Ramirez-Ruiz, E., Andrews, J. J., et al. 2019a, ApJ, 872, 105
Safarzadeh, M., Sarmento, R., & Scannapieco, E. 2019b, ApJ, 876, 28
Sales, L. V., Helmi, A., Abadi, M. G., et al. 2009, MNRAS, 400, L61
Schlafly, E. F., & Finkbeiner, D. P. 2011, ApJ, 737, 103
Schlaufman, K. C., & Casey, A. R. 2014, ApJ, 797, 13
Schlaufman, K. C., Thompson, I. B., & Casey, A. R. 2018, ApJ, 867, 98
Schlegel, D. J., Finkbeiner, D. P., & Davis, M. 1998, ApJ, 500, 525
Schönrich, R., Binney, J., & Dehnen, W. 2010, MNRAS, 403, 1829
Sestito, F., Buck, T., Starkenburg, E., et al. 2021, MNRAS, 500, 3750
Sestito, F., Longeard, N., Martin, N. F., et al. 2019, MNRAS, 484, 2166
Sestito, F., Martin, N. F., Starkenburg, E., et al. 2020, MNRAS, 497, L7
Shappee, B. J., Simon, J. D., Drout, M. R., et al. 2017, Sci, 358, 1574
Skrutskie, M. F., Cutri, R. M., Stiening, R., et al. 2006, AJ, 131, 1163
Smartt, S. J., Chen, T. W., Jerkstrand, A., et al. 2017, Natur, 551, 75
Sneden, C., Cowan, J. J., & Gallino, R. 2008, ARA&A, 46, 241
Spite, M., Caffau, E., Bonifacio, P., et al. 2013, A&A, 552, A107
Stancliffe, R. J., Church, R. P., Angelou, G. C., & Lattanzio, J. C. 2009, MNRAS, 396, 2313
Starkenburg, E., Martin, N., Youakim, K., et al. 2017b, MNRAS, 471, 2587
Starkenburg, E., Oman, K. A., Navarro, J. F., et al. 2017a, MNRAS, 465, 2212
Starkenburg, E., Shetrone, M. D., McConnachie, A. W., & Venn, K. A. 2014, MNRAS, 441, 1217
Steinmetz, M., Zwitter, T., Siebert, A., et al. 2006, AJ, 132, 1645
Suda, T., Aikawa, M., Machida, M. N., Fujimoto, M. Y., Iben, & Icko, J. 2004, ApJ, 611, 476
Tody, D. 1986, Proc. SPIE, 627, 733
Tody, D. 1993, in ASP Conf. Ser., 52, Astronomical Data Analysis Software and Systems II, ed. R. J. Hanisch, R. J. V. Brissenden, & J. Barnes (San Francisco, CA: ASP), 173
Tominaga, N., Iwamoto, N., & Nomoto, K. 2014, ApJ, 785, 98
van der Walt, S., Colbert, S. C., & Varoquaux, G. 2011, CSE, 13, 22
Vasiliev, E. 2019, MNRAS, 482, 1525
Venn, K. A., Irwin, M., Shetrone, M. D., et al. 2004, AJ, 128, 1177
Vincenzo, F., Spitoni, E., Calura, F., et al. 2019, MNRAS, 487, L47
Virtanen, P., Gommers, R., Oliphant, T. E., et al. 2020, NatMe, 17, 261
Wilson, E. B. 1927, J. Am. Stat. Assoc., 22, 209
Wright, E. L., Eisenhardt, P. R. M., Mainzer, A. K., et al. 2010, AJ, 140, 1868
Yanny, B., Rockosi, C., Newberg, H. J., et al. 2009, AJ, 137, 4377
Yong, D., Norris, J. E., Bessell, M. S., et al. 2013a, ApJ, 762, 26
Yong, D., Norris, J. E., Bessell, M. S., et al. 2013b, ApJ, 762, 27
Yoon, J., Beers, T. C., Dietz, S., et al. 2018, ApJ, 861, 146
Yoon, J., Beers, T. C., Placco, V. M., et al. 2016, ApJ, 833, 20
Yoon, J., Beers, T. C., Tian, D., & Whitten, D. D. 2019, ApJ, 878, 97
Yoon, J., Whitten, D. D., Beers, T. C., et al. 2020, ApJ, 894, 7
York, D. G., Adelman, J., John, E. J., et al. 2000, AJ, 120, 1579
Youakim, K., Starkenburg, E., Aguado, D. S., et al. 2017, MNRAS, 472, 2963
Youakim, K., Starkenburg, E., Martin, N. F., et al. 2020, MNRAS, 492, 4986
Yuan, Z., Myeong, G. C., Beers, T. C., et al. 2020, ApJ, 891, 39
Zhao, G., Mashonkina, L., Yan, H. L., et al. 2016, ApJ, 833, 225
Zhao, G., Zhao, Y.-H., Chu, Y.-Q., Jing, Y.-P., & Deng, L.-C. 2012, RAA, 12, 723